

Nowhere left to hide: revealing realistic gravitational-wave populations in high dimensions and high resolution with PIXELPOP.

Sofía Álvarez-López ,* Jack Heinzel , Matthew Mould , and Salvatore Vitale 

LIGO Laboratory, Massachusetts Institute of Technology, Cambridge, MA 02139, USA

Kavli Institute for Astrophysics and Space Research, Massachusetts Institute of Technology, Cambridge, MA 02139, USA and

Department of Physics, Massachusetts Institute of Technology, Cambridge, MA 02139, USA

(Dated: June 27, 2025)

The origins of merging compact binaries observed by the LIGO–Virgo–KAGRA gravitational-wave detectors remain uncertain, with multiple astrophysical channels possibly contributing to the merger rate. Formation processes can imprint nontrivial correlations in the underlying distribution of source properties, but current understanding of the overall population relies heavily on simplified and uncorrelated parametric models. In this work, we use PIXELPOP—a high-resolution Bayesian nonparametric model with minimal assumptions—to analyze multidimensional correlations in the astrophysical distribution of masses, spins, and redshifts of black-hole mergers from mock gravitational-wave catalogs constructed using population-synthesis simulations. With full parameter estimation on 400 detections at current sensitivities, we show explicitly that neglecting population-level correlations biases inference. In contrast, modeling all significant correlations with PIXELPOP allows us to correctly measure the astrophysical merger rate across all source parameters. We then propose a nonparametric method to distinguish between different formation channels by comparing the PIXELPOP results back to astrophysical simulations. For our simulated catalog, we find that only formation channels with significantly different physical processes are distinguishable, whereas channels that share evolutionary stages are not. Given the substantial uncertainties in source formation, our results highlight the necessity of multidimensional astrophysics-agnostic models like PIXELPOP for robust interpretation of gravitational-wave catalogs.

I. INTRODUCTION

Up to the end of their third observing run (O3), the LIGO [1], Virgo [2], and KAGRA [3] (LVK) gravitational-wave (GW) detectors have observed nearly 100 mergers of stellar-mass black holes (BHs) and neutron stars [4]. While GWs encode information such as the distance, masses, and spins of the compact objects they originate from, analyzing many observations jointly allows us to infer the underlying astrophysical population [5–10]. Broadly, the diverse range of astrophysical channels through which binary black-hole (BBH) systems may form are grouped into two categories [11–16]: (a) isolated binary evolution and (b) formation in dynamical environments.

In scenario (a), BBHs form in isolation from the binary evolution of their massive stellar progenitors. Such systems may undergo stable mass transfer (SMT) [17–20] or common-envelope (CE) phases [12, 13, 21–28], which tighten the orbit sufficiently to enable a merger within a Hubble time [29, 30]. Alternatively, if the progenitor stars are born in an already tight orbital configuration, tidal interactions can drive rapid stellar rotation, triggering chemically-homogeneous evolution (CHE) [31–35]. Despite only involving isolated binary evolution, CE and SMT share several evolutionary stages, while CHE binaries undergo significantly different physical processes.

In scenario (b), stellar and BH binaries in dense environments such as globular clusters (GCs) [36–48], nuclear

star clusters (NSCs) [38, 47, 49–51], and active galactic nuclei (AGN) disks [52–59] undergo strong gravitational encounters which dynamically assemble merging binary systems. Hierarchical formation of BBHs in triple and multiple massive-star systems [60–64] have also been predicted within these dense stellar environments.

To gain insight into the evolutionary channels shaping the population of binaries and infer the underlying distribution of BBHs from GW data, Bayesian hierarchical inference is the state-of-the-art approach [5–10]. This framework requires an input model for the underlying population, which is usually either parametric, astrophysically-informed, or flexible.

Heuristic parametric models describe the population using simple functional forms, perhaps with some astrophysical motivations. A few canonical examples include the POWER LAW + PEAK mass model [65] and the POWER LAW redshift model [66]. Parametric models also make strong assumptions about the underlying population, which may lead to model-driven conclusions, and their flexibility is limited by the functional forms they assume. As a result, they can introduce biases through model misspecification [67, 68].

Another approach is through astrophysically-informed or simulation-based models, which leverage astrophysical simulations as input to directly infer physically relevant quantities of stellar populations and binary evolution from GW data [18, 30, 68–78]. For instance, considering population synthesis simulations for five of the formation channels described above (CE, SMT, CHE, GC, and NSC), Zevin *et al.* [30] analyzed public LVK data from the second gravitational-wave transient cata-

* sofiaal@mit.edu

log (GWTC-2). They found strong support for multiple evolutionary mechanisms in the underlying astrophysical population of detected BBHs, with the majority of sources inferred to evolve with a CE episode, a preference for small natal BH spins, and large CE efficiencies. These conclusions were supported by Cheng *et al.* [68] and Colloms *et al.* [76] on GWTC-3 data. While simulation-based methods directly constrain the astrophysical parameters of these formation channels from GW data, they make the strongest assumptions about uncertain physical processes. This means that considering an incomplete set of formation channels contributing to the underlying BBH population or modeling the parameters with incorrect physical prescriptions can lead to significant biases [68].

At the other end of the spectrum, nonparametric models offer the greatest flexibility by minimizing prior assumptions and avoiding restrictive constraints on the inferred population (see, e.g., Refs. [79–94]). As a result, they are better able to uncover features that might otherwise be obscured by more rigid approaches, capturing the underlying astrophysical distribution of source properties with minimal bias. The downside is a bias-variance tradeoff, in that these models typically come with larger statistical uncertainties. Additionally, nonparametric models tend to be computationally expensive because—despite the name—they typically require inferring a larger number of parameters. Nonparametric models also lack interpretability due to their agnosticism about the underlying physics, although methods to reconstruct parametric models from nonparametric results have been proposed [95, 96].

Most nonparametric models are not designed to capture multidimensional correlations between source parameters, or to do so, must trade off resolution over the source parameter space due to the curse of dimensionality. Reducing the number of parameters can lower computational costs and allow for coarse-grained exploration of multidimensional structure. However, finer resolution is essential to capture the complex features and correlations that may be present in GW data. Failing to accurately model the population in multiple dimensions may obscure important astrophysical insights encoded in parameter correlations, which emerge naturally from the complex astrophysical processes governing formation channels [13, 14, 97–103]. Indeed, evidence for correlations has already been found in GW data [83, 104–113], albeit mostly contingent on simplified population modeling assumptions.

To resolve these shortcomings, Heinzel *et al.* [79, 107] introduced PIXELPOP, a high-resolution nonparametric algorithm used to infer joint astrophysical distributions of—and multidimensional correlations between—the properties of GW sources, making minimal prior assumptions about the underlying population. In this paper, we use PIXELPOP to assess the astrophysical conclusions that may be drawn using nonparametric Bayesian inference from GW data in a realistic setting. From Zevin

et al. [30], we use the population-synthesis simulations of BBH mergers that underwent CE evolution to construct a GW catalog. For each event, we perform full Bayesian parameter estimation (PE) at current detector sensitivities, as described in Sec. II. We pursue the following central questions:

1. ***Can we capture the complex, high-dimensional correlations expected in realistic astrophysical populations?***

PIXELPOP (described in Sec. IID) allows us to recover the high-dimensional correlations arising from the formation of realistic GW populations. However, doing so requires a highly sophisticated model that accounts for all significant correlations in the populations.

2. ***What is the effect of neglecting correlations between source parameters?***

Neglecting correlations can lead to observable bias in the inferred population already with catalog sizes as expected by the end of the fourth observing run (O4) [114] (Secs. III A and III B). In contrast, modeling all relevant correlations enables correct inference of the astrophysical merger rate across all source parameters, at the expense of increased computational cost and model complexity (Sec. III C).

3. ***Can we extract astrophysical insights from nonparametric inference?***

We propose a similarity metric (Sec. IV) to distinguish between different formation channels by comparing them to the PIXELPOP-inferred population. Considering our O4-like catalog, we find that a synthetic population consisting only of CE-driven BBH mergers is correctly favored over other formation channels with significantly different astrophysical processes (e.g., CHE). However, a purely CE population cannot be distinguished from a purely SMT population, likely due to the evolutionary stages shared between the two channels producing similar distributions of source properties.

We summarize our methods and results before concluding with future applications of this work in Sec. V.

II. METHODS

A. Population-synthesis simulations

We consider a population of BBH mergers that formed via CE evolution—found to be the dominant channel by some analyses of current GW data with simulation-based models [30, 68, 76]. We use simulations of binaries undergoing a late CE phase by Zevin *et al.* [30], which are based on the POSYDON framework [115] that integrates

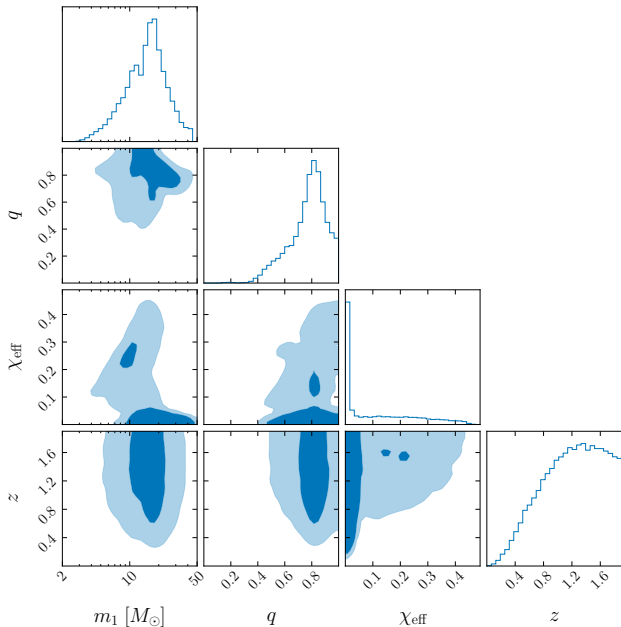


FIG. 1. One- and two-dimensional marginals of the source-frame primary mass m_1 , mass ratio q , effective spin χ_{eff} , and redshift z of the simulated CE population. The contours show the 50% and 90% credible regions.

population synthesis from COSMIC [116] with binary evolution calculations from MESA [117–121]. The resulting simulated population is parametrized by the natal BH spin χ_b and the CE ejection efficiency α_{CE} ; for our population we take $\chi_b = 0$ and $\alpha_{\text{CE}} = 1$, following Table 1 in Cheng *et al.* [68].

We model the population in a four-dimensional space consisting of the BH source-frame primary mass m_1 , binary mass ratio $q \in (0, 1]$, redshift z , and effective aligned spin [122]

$$\chi_{\text{eff}} = \frac{a_1 \cos \theta_1 + q a_2 \cos \theta_2}{1 + q} \in (-1, 1), \quad (1)$$

where a_1 and $a_2 \in [0, 1)$ are the dimensionless spin magnitudes, and θ_1 and θ_2 represent the spin–orbit misalignment of the primary and secondary components of the binary, respectively. Figure 1 shows the CE-simulated population in the parameter space spanned by m_1 , q , χ_{eff} , and z . These four parameters are non-trivially and nonlinearly correlated. Typical population analyses with simplistic parametrizations would struggle to capture such complexities, motivating our use of multidimensional Bayesian nonparametrics like PIXELPOP.

B. Quantifying pairwise correlations in the simulated population

To quantify the correlations in the simulated population (see Fig. 1), we use the pairwise mutual informa-

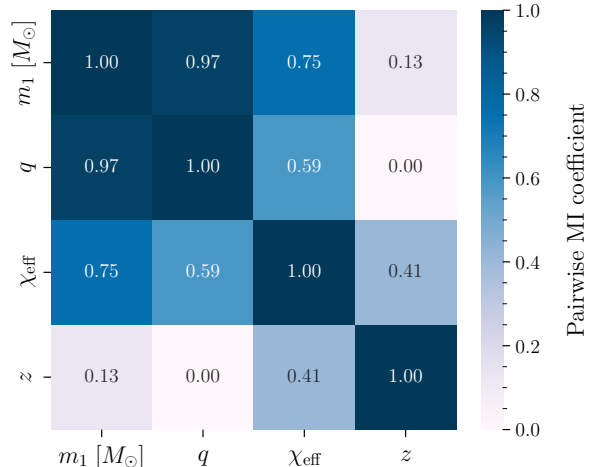


FIG. 2. Mutual-information correlation coefficient ρ_I over the four-dimensional parameter space of primary mass m_1 , mass ratio q , effective spin χ_{eff} , and redshift z for the CE population.

tion (MI) [123, 124]. The MI is a nonnegative real number that quantifies the shared information between two random variables. In terms of the Kullback–Leibler (KL) divergence, the pairwise MI quantifies the information gained when considering the joint distribution of two random variables over their independent marginals; the higher the MI, the stronger the correlation. The MI between random variables X and Y is defined as [125]

$$I(X, Y) = \int dx dy p_{XY}(x, y) \log \frac{p_{XY}(x, y)}{p_X(x)p_Y(y)}, \quad (2)$$

where $p_{XY}(x, y)$ is the joint probability density function (PDF) for X and Y , while $p_X(x)$ and $p_Y(y)$ are their univariate marginal distributions. In this paper, we use the MI since the correlations in our astrophysical population are neither linear nor monotonic. Therefore, the covariances and (most) correlation coefficients (e.g., Pearson or Spearman) are not sufficient to capture the behavior of such correlations. To allow for easier interpretation, the MI can be normalized to a correlation coefficient $\rho_I \in [0, 1]$:

$$\rho_I(X, Y) \equiv \sqrt{1 - e^{-2I(X, Y)}}, \quad (3)$$

such that $\rho_I(X, X) = \rho_I(Y, Y) = 1$ and $\rho_I(X, Y) = 0$ if and only if X and Y are independent. Note that this coefficient is an extension of the usual linear Pearson correlation coefficient [125].

Figure 2 shows the MI correlation coefficient for all parameter pairs in the four-dimensional space spanned by m_1 , q , χ_{eff} , and z , calculated using the **ennemi** package [125]. The MI coefficient indicates strong correlations

between m_1 and q , with $\rho_I(m_1, q) \approx 0.97$, as well as between m_1 and χ_{eff} with $\rho_I(m_1, \chi_{\text{eff}}) \approx 0.75$ and between q and χ_{eff} with $\rho_I(q, \chi_{\text{eff}}) \approx 0.59$. We also find a moderate correlation between χ_{eff} and z : $\rho_I(\chi_{\text{eff}}, z) \approx 0.41$. In contrast, note that $\rho_I(m_1, z) \approx 0.13$ and $\rho_I(q, z) \approx 0$, which means that both primary mass and mass ratio are nearly independent of redshift in the simulated population. In Sec. III, we use these MI coefficients to progressively find the subset of BBH source parameters with significant population-level correlations that must be captured with a multidimensional model to ensure unbiased inference.

C. Building a catalog of detectable sources

We build a set of $N_{\text{obs}} = 400$ GW events (consistent with near-future catalogs [114]) from the CE population, considering a GW interferometer network comprising both LIGO detectors and Virgo operating at O4 design sensitivity [126, 127]. We draw sources from the CE-simulated population and calculate their optimal network signal-to-noise ratio (SNR). We consider a BBH detected and add it to the catalog if $\rho_{\text{opt}} \geq 11$. We note that the optimal SNR implicitly depends on the true source parameters, so it is not a physical statistic on which to select detections [128]. However, the resulting systematic bias is expected to be small and largely masked by statistical uncertainty for catalog sizes with $\mathcal{O}(100)$ events, like ours [79].

For each of the BBHs in our catalog, we perform full parameter estimation (PE) to draw posterior samples of the source parameters. We use the IMRPhenomXP waveform model [129] and relative binning [130–133] (as implemented in the Bayesian-inference software *Bilby* [134]) to accelerate likelihood evaluations. We set uniform priors on redshift, dimensionless spin magnitudes $\in [0, 1]$, detector-frame chirp mass, and mass ratio q . We use isotropic priors for extrinsic parameters (e.g., sky location) and the spin tilts.

Applying a detection threshold to the simulated BBHs imposes a selection effect that we must account for [6, 135, 136]. We therefore perform a simulation campaign to characterize the sensitivity of the simulated O4 LIGO–Virgo network to BBHs spanning a range of parameters, as described in App. A. We then estimate the selection efficiency using Monte Carlo integration [137, 138].

D. Population inference

In this paper, we model the detection of GW signals as an inhomogeneous Poisson process [5, 6, 128, 136]. We directly infer the BBH merger rate $\mathcal{R}(\theta'; z)$, that is, the number N of mergers with source parameters θ' per unit

comoving volume V_c and source-frame time t_s :

$$\mathcal{R}(\theta'; z) = \frac{dN}{dV_c dt_s d\theta'}. \quad (4)$$

We emphasize that $\mathcal{R}(\theta'; z)$ evolves with redshift z , but does not correspond to a density in z . We model \mathcal{R} using *PIXELPOP*, following the procedure described in Sections II and III of Heinzel *et al.* [79]. The only modification we introduce here is the use of an intrinsic conditional autoregressive (ICAR) prior, a limiting special case of the conditional autoregressive (CAR) prior; we discuss the implemented changes in App. B.

With minimal astrophysical or parametric assumptions, *PIXELPOP* discretizes the joint space spanned by the source parameters into uniformly spaced bins, θ_b ($b = 1, \dots, B$), and infers the merger rate $\ln \mathcal{R}_b$ in each bin. The computational efficiency of *PIXELPOP* allows us to employ a much higher binning resolution than, e.g., binned Gaussian processes [10, 88], which makes it possible to resolve finer details in the population and to model more dimensions. This is crucial to reveal the multidimensional correlations in realistic astrophysical populations.

III. INFERRING MULTIDIMENSIONAL ASTROPHYSICAL POPULATIONS

A. Are two-dimensional correlations sufficient?

Figure 2 shows that m_1 and q are the most strongly correlated parameters in the CE population. Since studying different pairwise correlations is a common approach [107], we first use *PIXELPOP* to infer the two-dimensional merger-rate density $\mathcal{R}(m_1, q)$. We use 100 bins per dimension, following Heinzel *et al.* [79]. To model the remaining parameters, we leverage our knowledge of the true distributions (we discuss the implications of doing so in Sec. V). For redshift, we consider a *POWER LAW* model [66]. For the effective spin, we use a mixture model consisting of a narrow Gaussian to capture the sharp peak of the distribution (as seen in Fig. 1) and a Tukey window spanning the range $0 < \chi_{\text{eff}} < 0.5$ to capture the bulk; see Eq. (E.1) in Vitale *et al.* [139]. We refer to this as the *PEAK + TUKEY* model. The parameters and priors we used for these parametric models can be found in Table I. Note that the parametric models are independent from one another and from the merger rate over m_1 and q given by *PIXELPOP*. Overall, our model for the merger rate is given by:

$$\mathcal{R}(m_1, q, \chi_{\text{eff}}; z) = \mathcal{R}(m_1, q) p(\chi_{\text{eff}}) (1 + z)^\kappa. \quad (5)$$

On the left of Fig. 3, we show the inferred comoving merger-rate density $\mathcal{R}(m_1, q; z = 0.2)$ evaluated at a redshift of $z = 0.2$, marginalized over the effective-spin distribution. Note that *PIXELPOP* successfully recovers the underlying m_1 – q correlation. Additionally, in

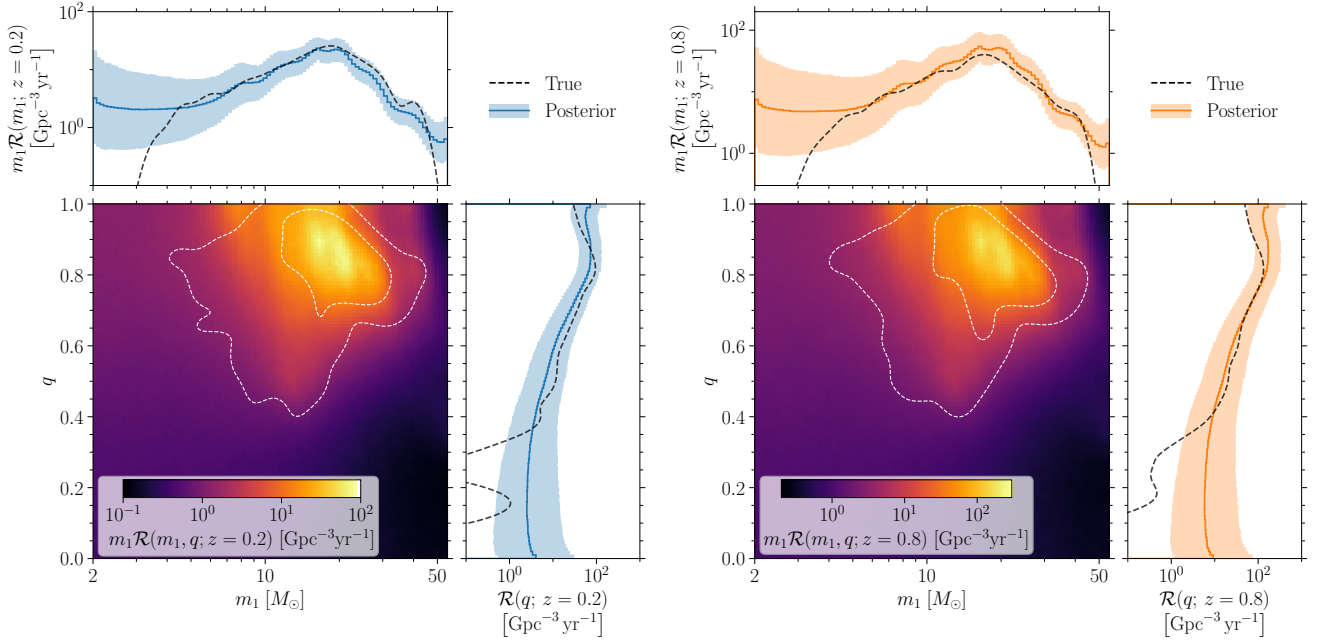


FIG. 3. *Left.* Comoving merger rate density $\mathcal{R}(m_1, q; z)$ inferred by PIXELPOP, evaluated at a fixed redshift $z = 0.2$. The central panel shows the median of the two-dimensional merger rate density, along with 50% and 90% credibility regions of the true population. Brighter regions indicate a higher merger rate. The upper and right-hand panels show the marginal merger rate density $\mathcal{R}(m_1; z = 0.2)$ and $\mathcal{R}(q; z = 0.2)$, respectively. The solid blue line shows the posterior median, with the central 90% credible region shaded. The dashed lines show the true underlying population, calculated using a kernel density estimate (KDE) scaled by the overall merger rate implied by the number of detections during the observing time. *Right.* Same as the left-hand panel, except at $z = 0.8$.

Parameter	Description	Prior
κ	z power-law index	$U(-2, 5)$
$\mu_{\chi_{\text{eff}}}$	Narrow Gaussian location	$U(-1, 0.05)$
$\sigma_{\chi_{\text{eff}}}$	Narrow Gaussian width	$U(0.0025, 0.1)$
T_{x0}	Tukey window center	$U(0.05, 1)$
T_k	Tukey window width	$U(0.1, 1)$
T_r	Tukey window shape	$U(0, 1)$
$\lambda_{\chi_{\text{eff}}}$	Fraction of sources in the χ_{eff} Gaussian component	$U(0, 1)$

TABLE I. Priors for the parameters of the PEAK + TUKEY spin model and POWER LAW redshift model. Uniform priors U are used for all parameters. In spin, the priors are defined to avoid degeneracies between the narrow component peaking at $\chi_{\text{eff}} \approx 0$ and the broader region of the distribution (see App. E in Vitale *et al.* [139] for details on the Tukey window parameters).

the upper and right-hand panels, we present the one-dimensional marginal merger rate densities $\mathcal{R}(m_1; z = 0.2)$ and $\mathcal{R}(q; z = 0.2)$, respectively. For both m_1 and q , PIXELPOP recovers the true distributions within the 90% posterior uncertainty except in regions where we would not expect $\gtrsim 1$ detection.

Note that our result deviates from the true population where the true merger rate is low (e.g., $m_1 \lesssim 3M_\odot$

and $q \lesssim 0.4$). This is characteristic of nonparametric models [79]: in particular, they overconfidently exclude merger-rates of $0 \text{ Gpc}^{-3} \text{ yr}^{-1}$ in the absence of informative data; e.g., in regions of low detectability (see discussion in Section IV of Heinzel *et al.* [79]). Additionally, note a slight increase in the inferred rate (and uncertainties) near the edges of parameter space (e.g., $q \approx 1$). Bins at the boundary of parameter space are coupled to fewer neighboring bins, meaning the uncertainty is generically larger, but larger by a symmetric amount in $\ln \mathcal{R}$. When we marginalize over a range of bins, we integrate over \mathcal{R} rather than $\ln \mathcal{R}$. The uncertainty thus becomes skewed to larger values at larger rates due to the nonlinearity of the exponential function.

Excluding prior-dominated regions, we quantify the precision of our inferred rates using the relative rates uncertainty given by the width of the central 90% credible interval $\Delta \mathcal{R}$ —within which we recover the true distributions—divided by the median inferred rate $\bar{\mathcal{R}}$. The smallest (largest) of these uncertainties corresponds to the most (least) precise measurement of the rate. Based on Fig. 3, we select $4 M_\odot \lesssim m_1 \lesssim 50 M_\odot$ and $0.4 \lesssim q \leq 1$ as the non-prior-dominated regions. In the case of primary mass, the rate with smallest relative uncertainty is $23_{-8}^{+12} \text{ Gpc}^{-3} \text{ yr}^{-1}$, near $m_1 \approx 16 M_\odot$. The width of the 90% posterior credible interval is thus $\Delta \mathcal{R} = 20 \text{ Gpc}^{-3} \text{ yr}^{-1}$, such that the smallest relative rate uncertainty is $\Delta \mathcal{R} / \bar{\mathcal{R}} = 0.9$. We report this value in Ta-

Model	Primary mass m_1		Mass ratio q	
	Smallest $\Delta\mathcal{R}/\bar{\mathcal{R}}$ (location)	Largest $\Delta\mathcal{R}/\bar{\mathcal{R}}$ (location)	Smallest $\Delta\mathcal{R}/\bar{\mathcal{R}}$ (location)	Largest $\Delta\mathcal{R}/\bar{\mathcal{R}}$ (location)
Two-dim. PIXELPOP	0.9 ($m_1 \approx 16 M_\odot$)	3.3 ($m_1 \approx 4 M_\odot$)	1.1 ($q \approx 0.9$)	2.9 ($q \approx 0.4$)
Three-dim. PIXELPOP	0.8 ($m_1 \approx 21 M_\odot$)	3.7 ($m_1 \approx 5 M_\odot$)	1.2 ($q \approx 0.9$)	3.5 ($q \approx 0.5$)
HYBRID PIXELPOP	0.8 ($m_1 \approx 21 M_\odot$)	3.1 ($m_1 \approx 4 M_\odot$)	1.2 ($q \approx 0.9$)	2.9 ($q \approx 0.4$)
Two-dim. PIXELPOP on GWTC-3 [107]	3.2 ($m_1 \approx 33 M_\odot$)	5.3 ($m_1 \approx 4 M_\odot$)	3.9 ($q \approx 0.8$)	5.9 ($q \approx 0.4$)
Fiducial parametric on GWTC-3 [10]	0.7 ($m_1 \approx 19 M_\odot$)	1.8 ($m_1 \approx 40 M_\odot$)	0.8 ($q \approx 0.8$)	1.9 ($q \approx 0.4$)

TABLE II. Smallest and largest relative rate uncertainties $\Delta\mathcal{R}/\bar{\mathcal{R}}$, together with the parameter values at which they occur in parentheses, for primary mass and mass ratio, evaluated at $z = 0.2$. Results are presented for the m_1 and q marginals of two-dimensional PIXELPOP (Sec. III A), three-dimensional PIXELPOP (Sec. III B), and HYBRID PIXELPOP (Sec. III C) models on the parameters of the simulated CE population. For reference, we also show the corresponding relative rate uncertainties obtained with the two-dimensional m_1 - q PIXELPOP study of GWTC-3 [107] and with the fiducial parametric POWERLAW+PEAKpopulation model used in GWTC-3 [10].

ble II, along with the largest relative rate uncertainty in m_1 (and the value at which it occurs). We also include the smallest and largest $\Delta\mathcal{R}/\bar{\mathcal{R}}$ (and locations) for mass ratio. To put these values in context, we compare our measurements to the relative rate uncertainties in GWTC-3 using (a) two-dimensional m_1 - q PIXELPOP as in Ref. [107] and (b) the fiducial POWERLAW + PEAK parametric model from Ref. [10] (fourth and fifth rows in Table II). Note that our relative uncertainties are narrower than those of model (a). In fact, our smallest values of $\Delta\mathcal{R}/\bar{\mathcal{R}}$ are similar to those of model (b). This is because we consider a catalog of 400 sources, comparable to the end of O4, which is almost six times larger than GWTC-3. However, our largest relative uncertainties are wider than in model (a) due to PIXELPOP being a more flexible model.

Next we evaluate the merger rate at $z = 0.8$, i.e., we consider $\mathcal{R}(m_1, q; z = 0.8)$. On the right panel in Fig. 3, note the inferred rate remains consistent with the true rate, even though we do not model the redshift evolution with PIXELPOP. The fact that we still recover the true distributions for m_1 and q suggests that these two variables are nearly independent of z . This behavior is consistent with the MI coefficients we calculated in Fig. 2: $\rho_I(m_1, z) \approx 0.13$ and $\rho_I(q, z) \approx 0$, implying that the m_1 - z and q - z correlations are negligible for the CE population.

While the two-dimensional m_1 - q PIXELPOP results appear unbiased, the parametric assumptions of Eq. (5) lead to major biases from the true population in effective spin. Using the PEAK + TUKEY parametrization, we do not correctly recover the true underlying distribution, as shown in Fig. 4. At both $z = 0.2$ and $z = 0.8$, the rate inferred with the PEAK + TUKEY model for $0 < \chi_{\text{eff}} < 0.5$ is below that of the true population, while the inferred rate for $\chi_{\text{eff}} \approx 0$ is overestimated. At the lower redshift value, we find that the true peak of the distribution (i.e., $\chi_{\text{eff}} \approx 0$) lies at the 2% level of the inferred merger rate. Additionally, in the bulk of the distribution, the largest deviation from the true merger rate occurs at $\chi_{\text{eff}} \approx 0.2$, where the inferred merger rate is inconsistent with the

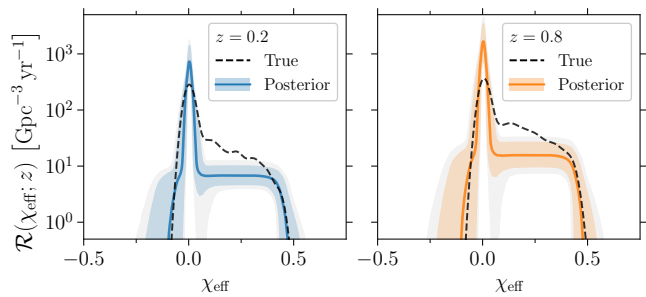


FIG. 4. Inferred merger-rate density $\mathcal{R}(\chi_{\text{eff}}; z)$ evaluated at redshifts $z = 0.2$ (left, in blue) and $z = 0.8$ (right, in orange). The solid line shows the posterior median, while the colored (gray) regions enclose the central 90% (99%) credible intervals. The dashed lines represent scaled KDEs of the true underlying population.

truth. The inconsistency between the true and inferred merger rates worsens at $z = 0.8$, both at $\chi_{\text{eff}} \approx 0$ and $\chi_{\text{eff}} \approx 0.2$.

The fact that we do not recover the underlying χ_{eff} distribution is not due to the specific choice of PEAK + TUKEY model. Rather, the bias arises from neglecting the m_1 - χ_{eff} and q - χ_{eff} correlations in Eq. (5), which are significant, as illustrated by the MI coefficients in Fig. 2. To verify that this is the source of bias, in App. C we artificially remove the correlations between the effective spin and the rest of the parameters and show that our parametric model is able to recover the behavior of the distribution with the 99% credible intervals. Therefore, we find that a two-dimensional PIXELPOP model is not sufficient and we need at least a three-dimensional model to capture the correlations in the simulated population.

B. Are three-dimensional correlations sufficient?

In the interest of capturing the three strongest correlations in the CE population, we now jointly model pri-

mary mass m_1 , mass ratio q , and effective spin χ_{eff} with PIXELPOP. By including χ_{eff} , we account for the m_1 – χ_{eff} and q – χ_{eff} correlations, which have the highest MI coefficients after the m_1 – q pair (see Fig. 2). Our bins are now three-dimensional (i.e., voxels). As 10^6 bins (100 bins per dimension) is computationally prohibitive, we reduce our binning resolution to 45 bins in each dimension, totaling $45^3 \approx 9 \times 10^4$ bins. Though decreasing the number of bins comes at the expense of reduced resolution, we found the above choice sufficient to resolve the joint and marginal distributions of the underlying population, as seen in the following. For redshift z , which is not modeled by PIXELPOP, we again use the POWER LAW redshift model, with priors in Table I. The overall model for the merger-rate density is now

$$\mathcal{R}(m_1, q, \chi_{\text{eff}}; z) = \mathcal{R}(m_1, q, \chi_{\text{eff}})(1+z)^\kappa. \quad (6)$$

To visualize the three-dimensional results, we calculate the two-dimensional marginal rates of each parameter pair, as well as the one-dimensional marginals.

Figure 5 shows the one- and two-dimensional marginals for the inferred merger-rate $\mathcal{R}(m_1, q, \chi_{\text{eff}}; z)$, evaluated at $z = 0.2$ (top row) and $z = 0.8$ (bottom row). PIXELPOP recovers the true m_1 and q distributions within the posterior uncertainty, except again in regions where we would not expect $\gtrsim 1$ detection. The second row in Table II shows the smallest and largest relative rate uncertainties we find for primary mass and mass ratio evaluated at $z = 0.2$. These $\Delta\mathcal{R}/\bar{\mathcal{R}}$ values are comparable or marginally larger than those obtained with two-dimensional PIXELPOP, consistent with the greater flexibility of the three-dimensional model.

At both $z = 0.2$ and $z = 0.8$, the inferred 90% credible interval successfully recovers the true mass ratio distribution in most of the $0 < q \leq 1$ range, excluding prior-dominated regions. However, we see small deviations from the 90% credible region for $0.5 \lesssim q \lesssim 0.7$. For instance, at the point of maximum deviation between the inferred and true rate, $q \approx 0.65$, we find that the truth lies at the 97% level of the inferred posterior distribution. In App. D, we show that these deviations are not attributable to model systematics. There, we run the analysis using point estimates for the properties of each event in our simulated catalog (i.e., in the absence of PE uncertainty) and recover the true mass-ratio distribution within the 90% uncertainty from PIXELPOP (see Fig. 14 in App. D).

At $z = 0.2$, the true effective spin distribution in the range $0 < \chi_{\text{eff}} \leq 0.5$ is now enclosed within the 90% credible interval inferred by PIXELPOP, which constitutes a significant improvement from the distribution obtained with the parametric PEAK + TUKEY model. We find that the smallest relative rate uncertainty in non-prior-dominated regions is $\Delta\mathcal{R}/\bar{\mathcal{R}} = 0.4$ at the peak of the distribution and the largest is $\Delta\mathcal{R}/\bar{\mathcal{R}} = 1.6$ near $\chi_{\text{eff}} \approx 0.3$.

However, at $\chi_{\text{eff}} \approx 0$, the merger rate inferred by PIXELPOP is lower than that of the true population. In fact, the true rate lies at the 99.9% level of the inferred pos-

terior distribution. This effect is clearer in the top-left panel of Fig. 6, which compares $\mathcal{R}(\chi_{\text{eff}}; z)$ at $z = 0.2$ (top) and $z = 0.8$ (bottom). In App. D, we show that this bias at the peak is due to the imperfect approximation of the likelihood for narrow populations. However, it is worth noting that the sharpness of the peak in the true distribution likely arises from assumptions in the underlying astrophysics [140], which might not reflect a true population, as discussed in Colloms *et al.* [76].

Additionally, there are no sources from the true population for $\chi_{\text{eff}} < 0$ and $\chi_{\text{eff}} > 0.5$, so PIXELPOP is only able to place an upper bound on the merger rate in these regions. Ideally, a model should infer a merger rate of nearly zero in regions of low detectability. However, as discussed before, it is challenging for nonparametric models to measure small merger rates.

At $z = 0.8$, the true value at the peak of the effective spin is now recovered within PIXELPOP’s uncertainty range: the true rate lies at the 87% level of the inferred merger rate posterior distribution. This is because the χ_{eff} distribution at $z = 0.8$ is slightly less steep from peak to trough than at $z = 0.2$, as shown in Fig. 7. In fact, the peak–trough rate ratio at $z = 0.8$ is ~ 0.5 times smaller than that at $z = 0.2$. However, for $0 < \chi_{\text{eff}} \leq 0.5$, the marginal χ_{eff} distribution at $z = 0.8$ deviates from the truth. This effect is more clearly seen in the bottom-left panels of Fig. 6. In fact, at $\chi_{\text{eff}} \approx 0.2$ —the point of maximum deviation between the inferred and true rate—we find that the truth lies at the 99% level of the inferred posterior distribution. As we show in App. D, when repeating the analysis using point estimates for the properties of each event, we *still* find that the true merger rate at $\chi_{\text{eff}} \approx 0.2$ lies at the 99% level of the inferred posterior distribution. The fact that the true χ_{eff} rate is recovered at lower (but not higher) values of redshift is a symptom of ignoring the χ_{eff} – z correlation. Indeed, the shape of the χ_{eff} merger rate density evolves with redshift, as shown in Fig. 7. This is also consistent with the non-negligible MI coefficient $\rho_I(\chi_{\text{eff}}, z)$ from Fig. 2. Therefore, we must model the χ_{eff} – z correlation.

C. Are all correlations necessary?

The natural next step would be to model all source parameters with PIXELPOP, which would allow us to effectively consider all correlations in our $(m_1, q, \chi_{\text{eff}}, z)$ parameter space. However, that is currently impractical for two main reasons. First, if we kept the same resolution as in three dimensions, in four dimensions we would now have 45 times more bins, i.e., $45^4 \approx 4.1 \times 10^6$ total bins. Additionally, we find that the approximations used to compute the population likelihood (see e.g., Refs. [5–10, 137, 138]) break down dramatically for four-dimensional PIXELPOP. With so many available pixels, it is inevitable that there will be some that contain one or more posterior samples from one of the observations but contain *no* samples for estimating the selection effi-

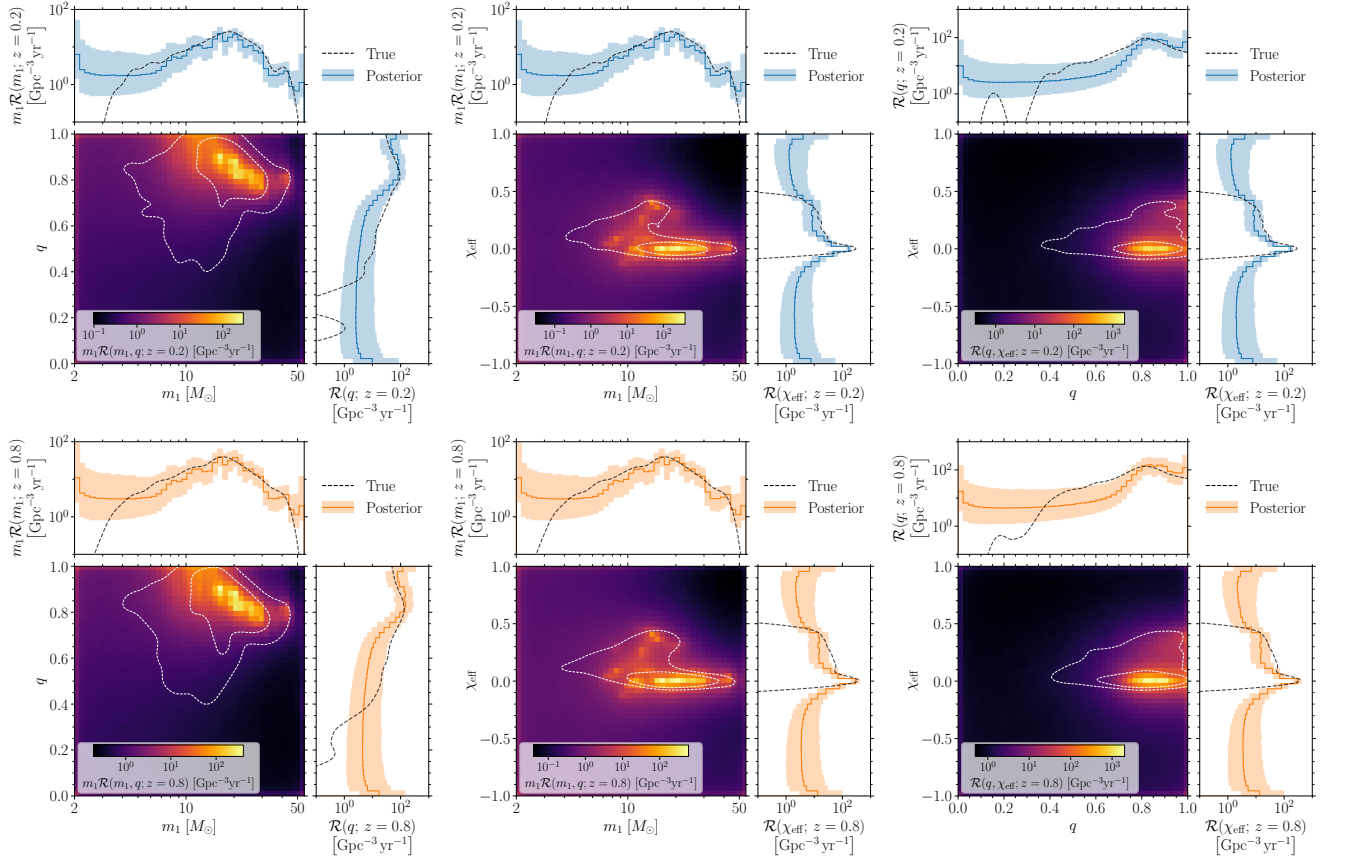


FIG. 5. For our three-dimensional PIXELPOP model, the inferred comoving merger-rate density $\mathcal{R}(m_1, q; z)$ (left), $\mathcal{R}(m_1, \chi_{\text{eff}}; z)$ (center), and $\mathcal{R}(q, \chi_{\text{eff}}; z)$ (right), evaluated at fixed redshifts $z = 0.2$ (top) and $z = 0.8$ (bottom). In each figure, the central panel shows the median of the two-dimensional merger-rate posterior, along with 50% and 90% credibility contours of the true underlying population of our simulated catalog; brighter regions indicate a higher inferred merger rate. Similarly, each upper (right-hand) panel shows the rate marginalized over the source parameter on the vertical (horizontal) axis; the dashed line represents the true population, while the solid line and shaded region represent the posterior median and central 90% credible region.

ciency. In that scenario, the likelihood estimator becomes unbounded, and the inferred rate in those bins diverges. It is possible that different approaches for evaluating the likelihood might be devised to avoid this issue, which we are exploring in ongoing work. An obvious solution that allows us to keep the same algorithm is to reduce the number of bins per dimension. We have decided not to follow that route because using fewer bins can wash out finer features in the population, e.g., the sharp peak in χ_{eff} . Instead, we have employed a hybrid approach that allows us to model all significant correlations in the population without increasing the dimensionality of PIXELPOP, as described below.

From Fig. 2, we have $\rho_I(m_1, z) \approx 0.13$ and $\rho_I(q, z) \approx 0$, which means that m_1 and q are nearly independent of z . On the other hand, there is a more significant correlation between χ_{eff} and z , with $\rho_I(\chi_{\text{eff}}, z) \approx 0.41$. Therefore, we consider a “semiparametric” approach: we use the parametric POWERLAW redshift evolution model from before, but attempt to capture the $\chi_{\text{eff}}-z$ correlation by modeling the redshift power-law index κ with a cubic spline,

$\kappa = \varphi(\chi_{\text{eff}})$. This allows us to encode a prior assumption that the merger rate evolves as a POWER LAW over redshift, but still with a flexible assumption about how this evolution depends on χ_{eff} . The spline consists of six evenly spaced nodes in the range $\chi_{\text{eff}} \in [-1, 1]$. The amplitude of each node is a hyperparameter of the model and is assigned a standard normal prior. With these considerations, our merger rate is modeled as

$$\mathcal{R}(m_1, q, \chi_{\text{eff}}; z) = \mathcal{R}(m_1, q, \chi_{\text{eff}})(1+z)^{\varphi(\chi_{\text{eff}})}. \quad (7)$$

Hereon, we refer to Eq. (7) as the HYBRID PIXELPOP model.

Figure 8 shows the inferred merger rate evaluated at $z = 0.2$ (top row) and $z = 0.8$ (bottom row). Like before, the one- and two-dimensional marginals over primary mass and mass ratio are consistent with both the true distributions and the inferred rates using the two- and three-dimensional PIXELPOP models, aside from small deviations not attributable to model systematics. At both redshift values, the true mass-ratio distribution in the range

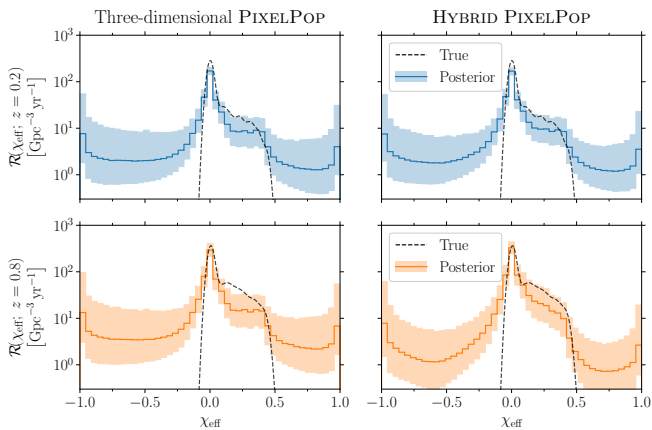


FIG. 6. Inferred merger-rate density $\mathcal{R}(\chi_{\text{eff}}; z)$ evaluated at redshifts $z = 0.2$ (blue) and $z = 0.8$ (orange) for three-dimensional PIXELPOP (left) and the HYBRID model (right), defined in Eqs. (6) and (7), respectively. The dashed line shows the true population, while the solid line and shaded region represent the posterior median and central 90% credible region.

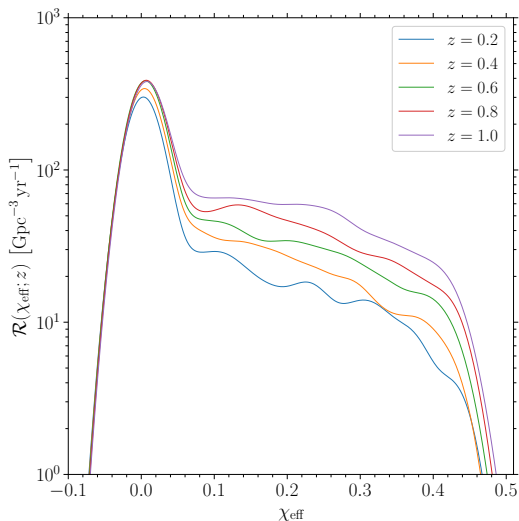


FIG. 7. Scaled KDEs of the merger rate $\mathcal{R}(\chi_{\text{eff}}; z)$ as a function of effective spin χ_{eff} , evaluated at redshifts $z \in \{0.2, 0.4, 0.6, 0.8, 1.0\}$. The shape of the distribution evolves with redshift.

$0.5 \lesssim q \lesssim 0.7$ is again slightly above the central 90% credible region. In fact, at $q \approx 0.65$, the truth lies at the 98% level of the inferred rate at both $z = 0.2$ and $z = 0.8$. However, similar to three-dimensional PIXELPOP, we do not find these deviations between the true and inferred rates with our catalog of point-estimate events (see discussion in App. D).

The minimum and maximum 90% relative rate uncertainties we recover for m_1 and q are shown in the third row of Table II. For the effective spin, we get similar relative uncertainties to those with three-dimensional PIXELPOP. The smallest (largest) $\Delta\mathcal{R}/\mathcal{R}$ is 0.4 (1.5) at

$\chi_{\text{eff}} \approx 0$ ($\chi_{\text{eff}} \approx 0.3$). Additionally, we still find a small deviation from the truth at the peak of the distribution: the true rate lies at the 99% level of the inferred rate. Again, this is due to the imperfect approximation of the likelihood for narrow populations (see App. D for further discussion).

The most significant result for the HYBRID PIXELPOP model with respect to the two- and three-dimensional PIXELPOP-only analyses is for the marginal effective spin distribution at $z = 0.8$. As shown in the bottom-right panel of Fig. 6, the inferred $\mathcal{R}(\chi_{\text{eff}}; z = 0.8)$ is now within the 90% credible interval for $0 \leq \chi_{\text{eff}} \leq 0.5$. We now find the true peak of the distribution at the 61% level of the inferred rate (compare to 100% in Sec. III A and 87% in Sec. III B). Additionally, at $\chi_{\text{eff}} \approx 0.2$ —the point of maximum deviation between the inferred and true rates in the earlier analyses—we now find that the truth lies at the 92% level of the inferred posterior distribution. This represents a significant improvement from three-dimensional PIXELPOP at $z = 0.8$, shown in the bottom-left panel of Fig. 6, where we observed a considerable bias due to the unmodeled $\chi_{\text{eff}}-z$ correlation. We further analyze this correlation in App. E by evaluating $\mathcal{R}(\chi_{\text{eff}}; z)$ at different values of the effective spin.

With the HYBRID PIXELPOP model, we recover the parameter distributions within the 90% posterior credible intervals, except for deviations from the truth not attributable to model systematics (see App. D). These results highlight that all significant correlations (for the CE population, all except the m_1-z and $q-z$ correlations) must be modeled to recover the merger rate across the parameter space with minimal bias.

IV. ARE FORMATION CHANNELS DISTINGUISHABLE?

The results we presented above show that PIXELPOP is a promising tool to measure the merger rate across a complicated *multidimensional* parameter space. However, this unmodeled inference alone does not provide information about the separate astrophysical formation channels that may contribute to the overall merger rate. In this section, we introduce a method to determine whether we can distinguish between different formation channels using the results from PIXELPOP.

Given a set of M synthetic sources whose true parameters $\{\theta_i\}_{i=1}^M$ are drawn from an astrophysical distribution $q(\theta)$, e.g., from a population-synthesis simulation (in our case, the CE population), the likelihood that they were instead independent draws from a different population model $p(\theta)$ is $p(\{\theta_i\}_{i=1}^M) = \prod_{i=1}^M p(\theta_i)$. The *similarity* of these two populations is encoded in the shape of their distributions across the parameter space of θ , not the number of simulated sources M . Therefore, we quantify the similarity $\mathcal{S}(p, q)$ with the average log-likelihood

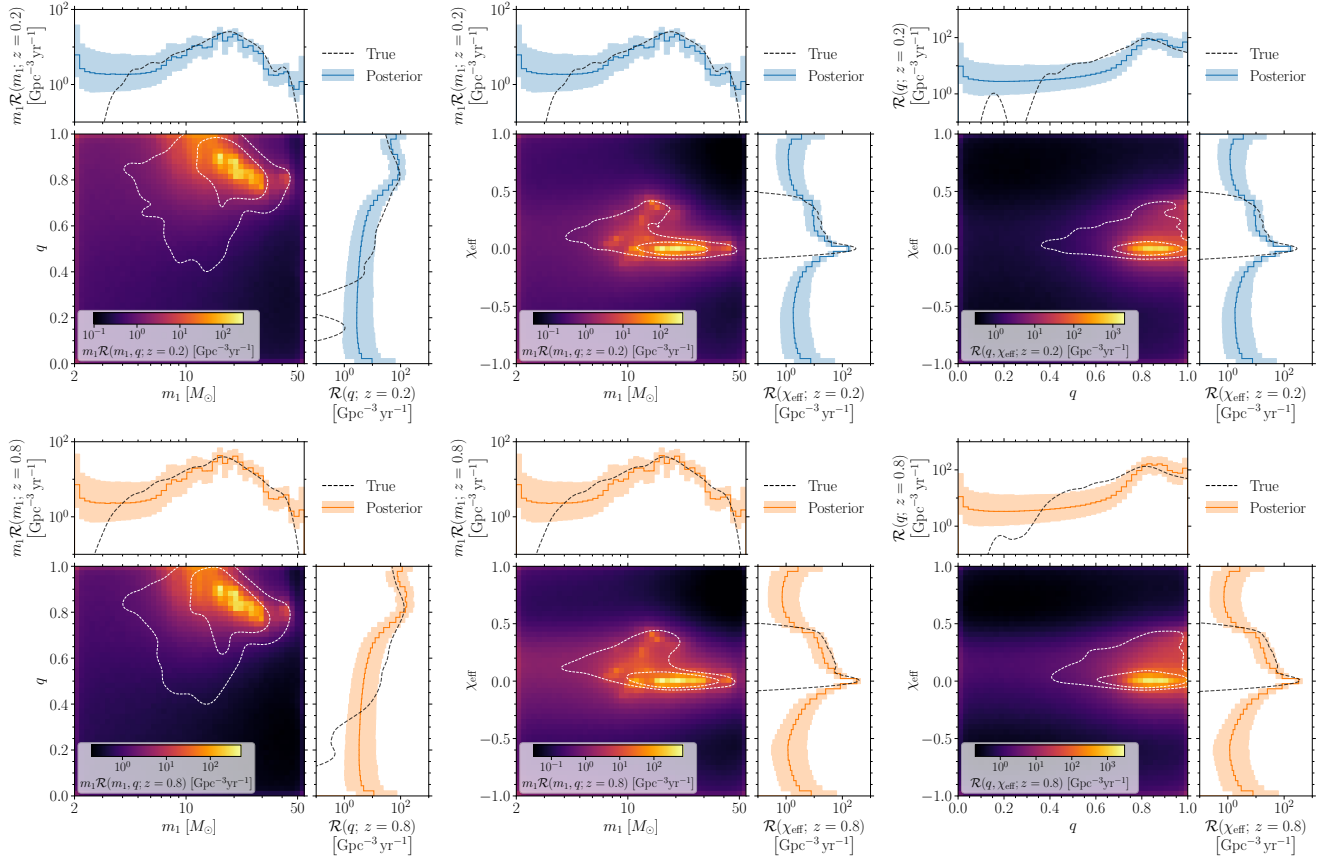


FIG. 8. Similar to Fig. 5, but for our HYBRID model: the inferred comoving merger-rate densities $\mathcal{R}(m_1, q; z)$ (left), $\mathcal{R}(m_1, \chi_{\text{eff}}; z)$ (center), and $\mathcal{R}(q, \chi_{\text{eff}}; z)$ (right), evaluated at redshifts $z = 0.2$ (top) and $z = 0.8$ (bottom). In each figure, the central panel shows the median of the two-dimensional merger-rate posterior, along with 50% and 90% credible regions of our true underlying population; brighter regions indicate a higher inferred merger rate. Similarly, each upper (right-hand) panel shows the rate marginalized over the source parameter on the vertical (horizontal) axis; the dashed line represents the true population, while the solid line and shaded region represent the posterior median and central 90% credible region.

$$\mathcal{S}(p, q) = \frac{1}{M} \sum_{i=1}^M \log p(\theta_i) \approx \int d\theta q(\theta) \log p(\theta). \quad (8)$$

To assess how well a proposed astrophysical population q matches an observed catalog of GW events, we use PIXELPOP to first encode our knowledge of the underlying population from which those events came without making strong assumptions. Specifically, we use the HYBRID PIXELPOP model for the reference distribution $p(\theta) \propto dN/d\theta$, where $\theta = (m_1, q, \chi_{\text{eff}}, z)$. Following Eq. (4), this is

$$p(m_1, q, \chi_{\text{eff}}, z) \propto \frac{1}{1+z} \frac{dV_c}{dz} \mathcal{R}(m_1, q, \chi_{\text{eff}}; z), \quad (9)$$

with an appropriate normalization constant and where $\mathcal{R}(m_1, q, \chi_{\text{eff}}; z)$ is the model defined in Eq. (7). From the population analysis with the HYBRID PIXELPOP model, we have many posterior draws that characterize the uncertainty in the merger rate, i.e., many different realizations of the model $p(m_1, q, \chi_{\text{eff}}, z)$. We compute Eq. (8)

for each of those posterior draws, thus constructing a posterior distribution for the population similarity. For two distinct astrophysical populations, their similarities to the HYBRID PIXELPOP model are correlated because they are computed using the same posterior draws. We can then use this similarity metric to assess whether the PIXELPOP inference results prefer the CE channel—the actual population that we used to produce our GW catalog—over other channels.

In particular, we compare the CE channel to two other isolated-binary populations simulated by Zevin *et al.* [30] and introduced in Sec. I: SMT and CHE. Similar to Fig. 1, in Fig. 9 we show the populations of SMT and CHE sources, in comparison to the CE population. Though these are all BBH isolated evolution channels, the astrophysical properties of the progenitors in CHE binaries (e.g., orbital periods $\lesssim 4$ days [13]) are significantly different from those of binaries undergoing CE or SMT evolution, which share several initial evolutionary stages. The key difference between these two channels is whether the mass transfer episode occurring after the first

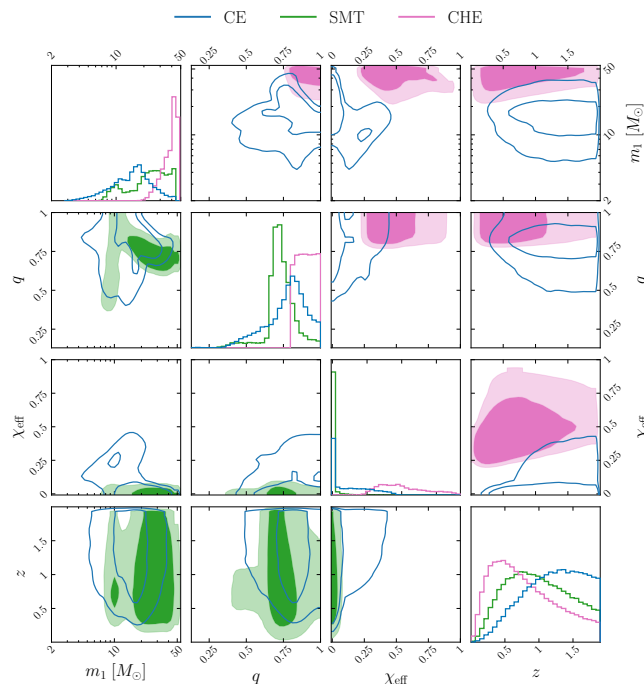


FIG. 9. One- and two-dimensional marginals of the source-frame primary mass m_1 , mass ratio q , effective spin χ_{eff} , and redshift z of the simulated CE (blue), SMT (green), and CHE (pink) populations. The contours show the 50% and 90% credible regions.

BH is born is stable or unstable [12, 30]. In the simulated populations we consider, binaries in the SMT channel experience only stable mass-transfer episodes, whereas those in the CE channel undergo a late CE phase.

In Fig. 10, we compare the posterior distributions of the population similarity for the CE population with those for the SMT and CHE populations. In regions below the diagonal, the CE population is more similar to the PIXELPOP inference and is favored over the alternative population considered. In contrast, regions above the diagonal indicate that a CE population is disfavored.

Compared to the CHE population, the true CE population is preferred with 100% credibility, meaning we can tell apart a universe in which all sources evolve via CE from one in which all sources evolve via CHE. Therefore, with an O4-like catalog of 400 detections, we can use Bayesian nonparametrics to distinguish certain GW formation channels. This conclusion is not too surprising, as these two formation channels produce very different source distributions due to substantially different astrophysical processes, as seen in Fig. 9. Here, we see that the population of CHE sources peaks at $m_1 \approx 44 M_\odot$, is uniformly distributed in mass ratio for $0.8 \leq q < 1$, has positive effective spins with no sharp features, and has a steeper redshift evolution, peaking at $z \approx 0.5$. In contrast, the CE population peaks at $m_1 \approx 19 M_\odot$, $q \approx 0.8$, and $z > 1$, and has a prominent peak at $\chi_{\text{eff}} \approx 0$. Since PIXELPOP analyzes joint distributions and multidimen-

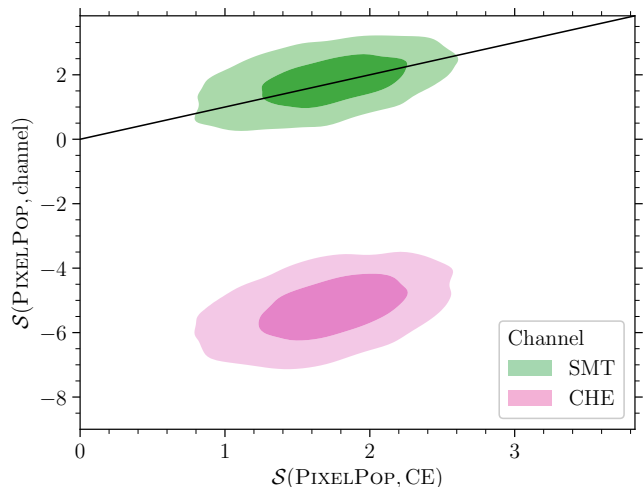


FIG. 10. Similarity of the simulated SMT (green) and CHE (pink) populations to the HYBRID model (vertical axis), compared to that of the true CE population (horizontal axis). Contours show the 50% and 90% credible regions over the similarities computed using posterior samples for the HYBRID population model. In regions below the diagonal line, the CE population is correctly concluded to be the true population.

sional correlations, it can correctly identify the differences between both populations, allowing us to conclude that CE is correctly preferred over CHE as the formation channel.

On the other hand, when we consider the simulated SMT population, we find that CE is favored over SMT at only 45% posterior credibility. In Fig. 10, this corresponds to more than half of posterior samples lying above the equal-similarity diagonal. This means that, at O4 sensitivity with a catalog of 400 CE sources, we cannot distinguish if the sources in the population evolved via CE or SMT alone. We attribute this result to CE and SMT being isolated binary evolution channels that share many evolutionary steps, even though they differ in some mass-transfer phases. Note from Fig. 9 that the mass-ratio distribution of the SMT population peaks at $q \approx 0.7$ (cf. $q \approx 0.8$ in the CE population) and it also has a sharp peak at $\chi_{\text{eff}} \approx 0$. The SMT m_1 - q correlation also resembles that of the CE population, along with the m_1 - χ_{eff} and q - χ_{eff} correlations. The indistinguishability between formation channels sharing several evolutionary steps using Bayesian nonparametrics highlights the difficulty of extracting astrophysical insights from these models.

V. CONCLUSIONS

In this paper, we used PIXELPOP [79, 107] to infer multidimensional correlations across the masses, spins, and redshifts of BBH mergers from a realistic astrophysical population of sources that evolved via CE. We consid-

ered a catalog of $N_{\text{obs}} = 400$ sources at O4 sensitivity with a three-detector network of LIGO and Virgo. Previous PIXELPOP analyses have focused on two-dimensional correlations only [79, 107]. However, due to the complex astrophysical processes governing CE evolution, the simulated population we considered here exhibits non-trivial and non-linear correlations across the four-dimensional space of primary BH mass m_1 , binary mass ratio q , effective spin χ_{eff} , and merger redshift z .

We employed the mutual information (MI) to quantify the degree of correlation between source properties in the population, finding that the most correlated pairs in our simulated population are (in descending order): (m_1, q) , (m_1, χ_{eff}) , (q, χ_{eff}) , and (χ_{eff}, z) . Therefore, we followed a multi-step approach to infer the underlying population and its correlations, using PIXELPOP to prevent imposing strong *a-priori* assumptions. By progressively allowing for population-level correlations in our analyses, we illustrate the biases that can arise from using insufficient models: (1) we modeled the m_1 – q correlation with PIXELPOP, but used univariate parametric models for χ_{eff} and z , which led to significant biases due to the unmodeled correlations involving effective spin (Sec. III A); (2) we included the correlations between χ_{eff} and mass parameters, but still found deviations from the truth for the inferred effective spin distribution at higher redshift due to the significant—yet unmodeled—evolution of χ_{eff} with z (Sec. III B); (3) finally, besides modeling $(m_1, q, \chi_{\text{eff}})$ with PIXELPOP, we used a hybrid approach to account for the correlation between χ_{eff} and z by taking advantage of the near independence of m_1 and q with redshift (Sec. III C).

With the HYBRID model, we successfully recover the astrophysical merger rate in all source parameters with no bias, aside from small deviations from the 90% credible region not attributable to model systematics (see App. D for further discussion). **These results highlight PIXELPOP’s capability of inferring population-level correlations for large catalogs of realistic sources.** However, in pursuing our multi-step approach, we utilized our knowledge of the true population. With real GW observations, we cannot *a-priori* ignore any (potential) correlations in the underlying population. The posteriors for our three models all passed one-dimensional posterior predictive checks, even though we know the two- and three-dimensional PIXELPOP models are not correctly inferring the underlying population. Indeed, previous work has shown that standard posterior predictive checks often fail [67, 141], and we will therefore pursue more robust checks that account for correlations in future work.

Having a model that accounts for all significant correlations with no bias allowed us to test whether meaningful astrophysical insights can be extracted from the inference results. While nonparametric models generally lack interpretability, **we devised a model-independent method to compare the *similarity* of proposed astrophysical populations with the nonparametric**

results from PIXELPOP. With current sensitivities and near-future catalogs, we found that only channels with significantly different astrophysical processes can be distinguished.

In particular, considering a BBH population in which all binaries undergo a late CE phase, we found that CE is correctly favored as the dominant evolutionary mechanism over CHE due to the distinct correlations imprinted by both formation channels. On the other hand, we found that it is not possible to distinguish whether the BBHs in the underlying population evolved via CE or SMT alone. This is because both channels share several evolutionary stages, which imprint similar features in the multidimensional correlations, making them difficult to tell apart with a nonparametric model. In this way, similar formation channels remain undistinguishable under nonparametric analyses at current sensitivity with near-future catalogs. Our results contrast sharply with those from astrophysically informed population models [30, 76]: while these can confidently infer the branching fractions of formation channels in BBH populations, they also rely on strong assumptions that we cannot make in reality, which can lead to highly biased results (See e.g., Ref. [68]). Since we cannot distinguish between populations where all sources evolve via one particular channel, we have even less chance of probing mixtures of populations in a nonparametric way, which is why we did not consider true populations consisting of a mixture of different formation channels. In future work, we plan to extend the similarity metric to account for populations originating from multiple formation channels.

With the anticipated increase in sensitivity of ground-based GW detectors over the next few years, BBH catalogs are expected to expand well beyond the datasets considered in this paper. By the conclusion of the fifth observing run, there may be more than 1000 BBH observations [142]. Such a substantial dataset may allow us to resolve population-level differences that are currently elusive, as we showed in this paper. For example, the CE and SMT formation channels—which we found to be indistinguishable with a sample of 400 BBHs—may become distinguishable as subtle statistical features emerge with a larger number of sources. To maximize our ability to uncover these features, the development of algorithms capable of inferring the high-dimensional structure of the parameter space is crucial. PIXELPOP represents an important step in that direction.

ACKNOWLEDGMENTS

We thank Cailin Plunkett, Thomas Dent, and Noah Wolfe for useful discussions. We also thank Storm Collopy as our internal LIGO reviewer. S.A.-L. is supported by the Mario Santo Domingo and Thomas A. Frank fellowship funds at MIT. J.H. is supported by the NSF Graduate Research Fellowship under Grant No. DGE1122374. M.M. is supported by the LIGO Labo-

ratory through the National Science Foundation awards PHY-1764464 and PHY-2309200. J.H. and S.V. are partially supported by the NSF grant PHY-2045740. The authors are grateful for computational resources provided by the LIGO Laboratory and supported by National Science Foundation Grants PHY-0757058 and PHY-0823459.

Appendix A: Sensitivity injections

To account for selection effects when recovering the CE population, we perform a simulation campaign to characterize the sensitivity of the O4 LIGO–Virgo network to BBHs spanning a range of parameters. We draw the BBH injections from the following distributions: a POWER LAW redshift model [66], a mixture of two Gaussian distributions for the effective spin: one narrow for the peak at $\chi_{\text{eff}} \approx 0$ and one wide for the bulk of the distribution. We use a normalizing flow [143, 144] implemented with FLOWJAX [145] to approximate the two-dimensional m_1 – q distribution and draw 80% of the injections from it. Our normalizing flow consists of only three coupling layers with affine transformations [146], each using a conditioner network with two hidden layers of 10 ReLU-activated neurons. We sample the remaining 20% of the sources from uniform joint distributions in $\log m_1$ and q . For all the other parameters, we sample from the same priors as used for PE. We draw a total of 8.5×10^8 sources, 2×10^6 of which are above our SNR threshold of $\rho_{\text{opt}} = 11$, as in Sec. II C.

Appendix B: The intrinsic conditional autoregressive (ICAR) model

In our original implementation introduced in Ref. [79], we used a CAR prior for the binned multi-dimensional rate density. The CAR prior is given as [147, 148]:

$$p(\ln \mathcal{R} | \kappa, \sigma, \mu) = \sqrt{\frac{\det(\mathbf{D} - \kappa \mathbf{A})}{(2\pi\sigma^2)^B}} \times \exp \left[-(\ln \mathcal{R} - \mu \mathbf{I})^T \frac{\mathbf{D} - \kappa \mathbf{A}}{2\sigma^2} (\ln \mathcal{R} - \mu \mathbf{I}) \right], \quad (\text{B1})$$

where: \mathcal{R} is a vector representation of all the multi-dimensional binned rates $\{\mathcal{R}_b\}_{b=1}^B$, \mathbf{I} is a vector of ones; \mathbf{A} is the adjacency matrix, where $A_{ij} = 1$ if the i^{th} and j^{th} bins are adjacent and 0 otherwise; and \mathbf{D} is a diagonal matrix in which the diagonal entries are the number of adjacent sites to each bin. The CAR model is conditional on three parameters: κ , σ , and μ . The mean μ and the coupling parameter σ set the global scale and variation of \mathcal{R} , respectively. The correlation parameter $\kappa \in [0, 1]$ determines the coupling between neighboring bins. In particular, when $\kappa = 1$, adjacent bins are conditionally coupled, while at $\kappa = 0$ neighboring bins are independent of each other (See Ref. [79] for more details). The

CAR model is much more efficient to evaluate than, e.g., a Gaussian process prior, because the covariance matrix determinant is trivial after evaluating the eigenspectrum of $\mathbf{D}^{-1}\mathbf{A}$, whereas the Gaussian process requires a matrix inversion and determinant at every evaluation. However, the large number of bins requires computing this eigenspectrum for a very large matrix: for models with $\mathcal{O}(10^5)$ bins total considered here, this can take days.

In this work, we instead use a CAR model in the limit of $\kappa \rightarrow 1$, also known as an ICAR model. Indeed, we noticed in Refs. [79, 107] that the posterior on κ for the GW population inference problem peaked strongly at 1, i.e., the GW population is more easily explained by coupling the neighboring bins. In the ICAR limit, the probability density becomes independent of μ and may be written

$$p(\{\ln \mathcal{R}_b\} | \sigma) \propto (2\pi\sigma^2)^{-B/2} \times \exp \left[- \sum_{i < j \text{ adjacent}} \frac{(\ln \mathcal{R}_i - \ln \mathcal{R}_j)^2}{\sigma^2} \right]. \quad (\text{B2})$$

where the sum inside the exponential is performed over unique pairs of adjacent bins. The probability density in Eq. (B2) is invariant to a constant shift to the $\ln \mathcal{R}$ vector, which implies the prior does not have finite normalization (i.e., it is an improper prior). In fact, we drop the determinant term (which normalizes the distribution), since the matrix $\mathbf{D} - \mathbf{A}$ is singular and therefore has determinant zero. The determinant $\det(\mathbf{D} - \kappa \mathbf{A})$ is only a constant in the prior, and hence we can drop this term in the prior without affecting the PIXELPOP posterior for inference with fixed κ . This justifies the removal of the normalization term $\det(\mathbf{D} - \mathbf{A}) = 0$. The scale for $\ln \mathcal{R}$ is set by the likelihood function during inference, which makes the Bayesian posterior a well-defined probability distribution with a finite normalization.

Appendix C: Removing correlations as a sanity check

In Section III A, we modeled the most correlated parameter pair (m_1, q) with two-dimensional PIXELPOP and we observed significant biases in the effective spin distribution recovered with the PEAK + TUKEY parametric model. Here, we find that the model misspecifications discussed in Section III A arise from neglected correlations in the population—especially those involving χ_{eff} —rather than from limitations in the assumed parametric model for the effective spin. To confirm the source of the bias, we artificially remove all correlations in the population except that between m_1 and q . We rerun full PE and repeat the procedure of Sec. II C to get a catalog of $N_{\text{obs}} = 400$ detections. For inference, we again model the merger rate $\mathcal{R}(m_1, q, \chi_{\text{eff}}; z)$ as defined in Eq. (5).

Similar to Fig. 3, we recover the one- and two-dimensional comoving merger-rate densities for the parameters inferred with PIXELPOP at both $z = 0.2$ and $z = 0.8$ within the 90% credible regions. Figure 11 shows

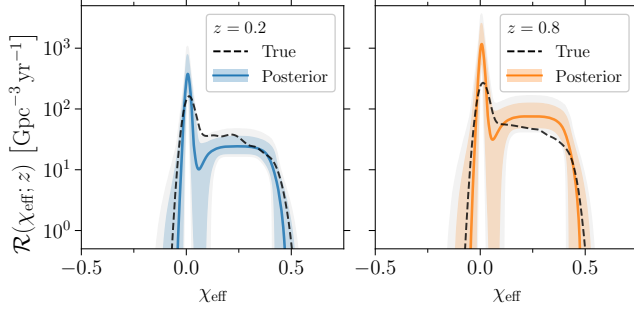


FIG. 11. Inferred merger-rate density $\mathcal{R}(\chi_{\text{eff}}; z)$ at redshifts $z = 0.2$ (left, in blue) and $z = 0.8$ (right, in orange) with the PEAK + TUKEY model on the population with artificially removed correlations. Compared to Fig. 4, the true distribution (dashed lines) is now within the 99% credible interval (shaded gray region) of the inferred rate.

the one-dimensional effective-spin distribution inferred with the PEAK + TUKEY model at $z = 0.2$ and $z = 0.8$, along with 90% and 99% credible intervals. Compared to Fig. 4, we now recover the true one-dimensional effective-spin distribution.

When studying the fully correlated scenario with two-dimensional PIXELPOP in Sec. III A, we found that at $\chi_{\text{eff}} \approx 0.2$ —the effective spin value in the broad component of the distribution with maximum deviation between the inferred and true rate—the posterior was inconsistent with the truth at both $z = 0.2$ and $z = 0.8$. Here, we find that the truth lies at the 97% ($z = 0.2$) and 6% ($z = 0.8$) levels of the inferred rate. Therefore, ignoring the correlations between effective spin and the other parameters is the primary driver of the biased inference we saw in Section III A.

Appendix D: Results in the absence of single-event uncertainty

Besides performing the inference on the catalog of detectable sources described in Sec. II C, we also consider a set of $N = 400$ events with point-estimates of the true values of the source properties (i.e., in the limit of no PE uncertainty). Our purpose with these analyses is three-fold: (a) to confirm that, in the absence of PE uncertainty, we get tighter or comparable constraints for the inferred merger rate; (b) to highlight that the bias at $\chi_{\text{eff}} \approx 0$ found in Fig. 6 is a result of the imperfect Monte Carlo approximation of the likelihood for populations with very narrow features; and (c) to show that small deviations from the 90% credible interval in the mass-ratio distribution (see Fig. 5 and Fig. 8) are not attributable to model systematics.

Regarding (a), in the absence of PE uncertainty, we recover the true distributions of all source parameters with narrower or similar credibility regions. To illustrate this, we consider the case in which we only model the (m_1, q)

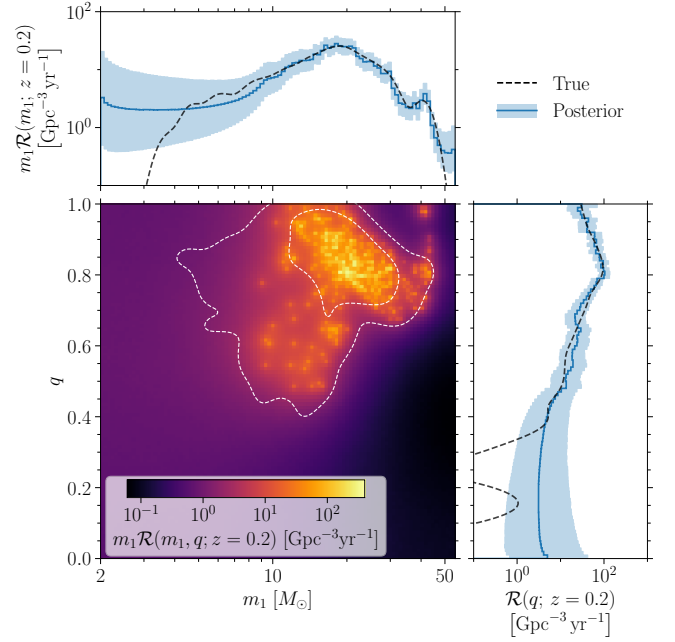


FIG. 12. Inferred comoving merger-rate density $\mathcal{R}(m_1, q; z = 0.2)$ for the catalog of events with point estimates for their source properties; otherwise, the same as the left panel in Fig. 3.

correlation and, therefore, can achieve higher resolution in the parameter space (100 bins per dimension). Just like the left plot of Fig. 3, Fig. 12 shows $\mathcal{R}(m_1, q; z = 0.2)$ (central panel), along with $\mathcal{R}(m_1; z = 0.2)$ (top), and $\mathcal{R}(q; z = 0.2)$ (right). The joint distribution shows finer features of the complex m_1 - q correlation. In general, we find better (comparable) constraints for the smallest (largest) relative rate uncertainty. For m_1 , we find $\Delta\mathcal{R}/\bar{\mathcal{R}} = 0.6$ near $m_1 \approx 22 M_\odot$. The largest is 3.2 at $m_1 \approx 4 M_\odot$. For mass ratio, we find that the largest relative rate is $\Delta\mathcal{R}/\bar{\mathcal{R}} = 2.8$ (near $q = 0.4$) whereas the smallest is 0.6 (at $q \approx 0.8$). This is approximately half the smallest relative rate calculated in Sec. III A, as expected in the limit of no PE uncertainty.

For (b), we confirm that the bias in the peak of the effective spin distribution seen in Fig. 6 is due to the imperfect approximation of the likelihood to narrow populations. We run three-dimensional PIXELPOP and HYBRID models using point estimates for the properties of each event in our simulated catalog. Similar to Fig. 6, Fig. 13 shows the inferred marginalized rate $\mathcal{R}(\chi_{\text{eff}}; z)$ at $z = 0.2$ and $z = 0.8$, with the three-dimensional PIXELPOP analysis on the left and the HYBRID model on the right. Just like in the analysis with full PE, at $z = 0.8$ we recover the χ_{eff} peak at the 65% and 32% levels for three-dimensional PIXELPOP and for HYBRID PIXELPOP, respectively. At $z = 0.2$, the true value of the peak is now within the 90% credible interval for both the three-dimensional PIXELPOP and the HYBRID PIXELPOP model. We find that the truth lies at the 63% and 80% level of the inferred pos-

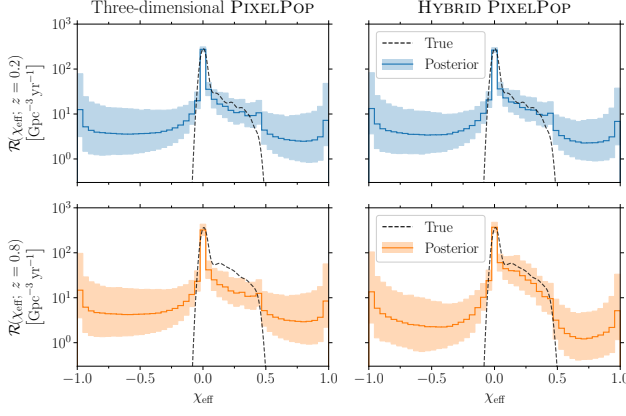


FIG. 13. Inferred marginalized merger-rate density $\mathcal{R}(\chi_{\text{eff}}; z)$ at redshifts $z = 0.2$ (blue) and $z = 0.8$ (orange) for the three-dimensional PIXELPOP (left) and HYBRID (right) models, using the catalog of point-estimate events. Otherwise, similar to Fig. 6. In this case, any deviation from the truth in the peak of the effective-spin distribution at $\chi_{\text{eff}} \approx 0$ is minimal. However, there is significant bias at $z = 0.8$ in the $0 < \chi_{\text{eff}} \leq 0.5$ region.

terior distribution, respectively. Therefore, we see that the bias in Fig. 6 is due to the imperfect Monte Carlo approximation of the likelihood for narrow features in the population [137, 138].

At $z = 0.8$, with three-dimensional PIXELPOP, we still find the bias in effective spin described in Sec. IIIC for the bulk of the distribution ($0 < \chi_{\text{eff}} < 0.5$). In fact, at $\chi_{\text{eff}} \approx 0.2$, where the inferred rate deviates most from the truth, the true merger rate lies at the 99% level of the inferred merger rate posterior distribution. This confirms that we do not recover the entirety of the effective spin distribution with three-dimensional PIXELPOP because we inherently neglect the $\chi_{\text{eff}}-z$ correlation in this analysis.

Regarding (c), in Figs. 5 and 8 we found small deviations of our inferred mass-ratio distribution from the truth at $\approx 90\%$ credibility. Here, we run our three-dimensional PIXELPOP and HYBRID models on point estimates for the properties of each event in our simulated catalog. Figure 14 shows the inferred marginalized rate $\mathcal{R}(q; z)$ at $z = 0.2$ (top row) and $z = 0.8$ (bottom row) for the three-dimensional PIXELPOP model (left column) and the HYBRID model (right column) in the absence of single-event PE uncertainty. As expected, we still find deviations from the truth at $q \lesssim 0.4$ due to the absence of informative data in this region. However, in contrast with the analyses on full PE, we now find that for both models at any redshift the true distribution in the region $q \gtrsim 0.4$ is now within the 90% credible interval. Therefore, we confirm that the deviations in Figs. 5 and 8 are not attributable to model systematics.

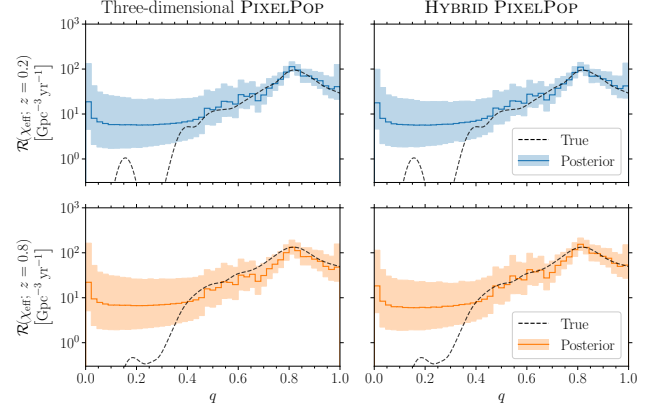


FIG. 14. Inferred marginalized merger-rate density $\mathcal{R}(q; z)$ at redshifts $z = 0.2$ (blue) and $z = 0.8$ (orange) for the three-dimensional PIXELPOP (left) and HYBRID (right) models, using the catalog of point-estimate events. The dashed line represents the true population, while the solid line and shaded region represent the posterior median and central 90% credible region. There are no deviations between the inferred and true rate in the $0.5 \lesssim q \lesssim 0.7$ region.

Appendix E: Studying the $\chi_{\text{eff}}-z$ correlation with the HYBRID model

Using the HYBRID model defined in Eq. (7), we can study the $\chi_{\text{eff}}-z$ correlation in the simulated CE population. This is the only model we can use to study such correlation because the two- and three-dimensional PIXELPOP models assume independence between redshift and effective spin. Figure 15 shows the merger-rate density $\mathcal{R}(\chi_{\text{eff}}; z)$ at $\chi_{\text{eff}} \approx 0$ (the peak), $\chi_{\text{eff}} \approx 0.05$ (just to the right of the peak), and $\chi_{\text{eff}} \approx 0.2$ (in the broad component of the effective spin distribution).

Note that the inferred merger-rate density $\mathcal{R}(\chi_{\text{eff}}; z)$ is consistent with the truth within the central 90% posterior uncertainty at both $\chi_{\text{eff}} \approx 0.05$ and $\chi_{\text{eff}} \approx 0.2$. At these values, the flexibility of the spline that models the power-law index of the redshift evolution as a function of χ_{eff} is sufficient to capture the behavior of the true distribution. However, $\mathcal{R}(\chi_{\text{eff}} \approx 0; z)$ (top panel) is only consistent within the 90% credible interval for $z \lesssim 1$. For $z \gtrsim 1$, we see a significant deviation from the truth in the inferred merger rate evolution, which we also find when considering point estimates for the source properties of events in our catalog. The observed bias results from the redshift dependence on the effective spin evolving more steeply around the $\chi_{\text{eff}} \approx 0$ peak than allowed for by our χ_{eff} -dependent spline model for the redshift power-law index. There is a visible difference in the shape of $\mathcal{R}(\chi_{\text{eff}}; z)$ at $\chi_{\text{eff}} \approx 0$ and $\chi_{\text{eff}} \approx 0.05$. In the first case, the true merger rate decreases with redshift for $z \gtrsim 0.5$ while in the second case, the true merger rate monotonically increases with redshift. Additionally, due to the binning we use in the HYBRID model (i.e., 45 bins for the effec-

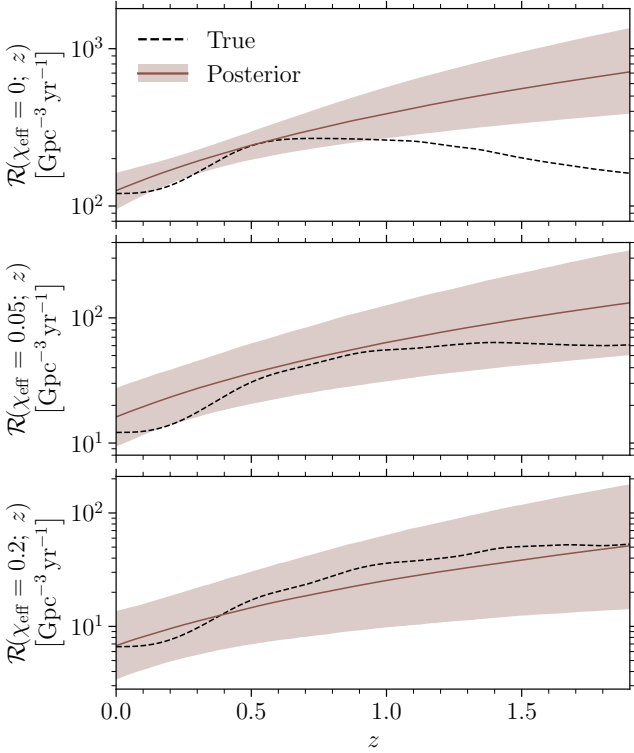


FIG. 15. Inferred evolution of the merger-rate density $\mathcal{R}(\chi_{\text{eff}}; z)$ over redshift and as a function of the effective spin $\chi_{\text{eff}} \approx 0$ (top), 0.05 (middle), and 0.2 (bottom). The inferred median and central 90% credible region are given by the solid line and shaded areas, respectively, while the underlying evolution of the true population is given by the dashed black line.

tive spin), $\chi_{\text{eff}} \approx 0$ and $\chi_{\text{eff}} \approx 0.05$ lie in different bins. To better resolve the fast evolution of the redshift distribution near the effective spin peak, we aim to explore in the future the use of adaptive binning for PIXELPOP. This technique would allow to resolve with finer bins the area around the narrow χ_{eff} peak and possibly recover $\mathcal{R}(\chi_{\text{eff}} \approx 0; z)$ closer to the true merger rate.

-
- [1] J. Aasi *et al.* (LIGO Scientific), *Class. Quant. Grav.* **32**, 074001 (2015), arXiv:1411.4547 [gr-qc].
 - [2] F. Acernese *et al.* (VIRGO), *Class. Quant. Grav.* **32**, 024001 (2015), arXiv:1408.3978 [gr-qc].
 - [3] T. Akutsu *et al.* (KAGRA), *PTEP* **2021**, 05A101 (2021), arXiv:2005.05574 [physics.ins-det].
 - [4] R. Abbott *et al.* (KAGRA, VIRGO, LIGO Scientific), *Phys. Rev. X* **13**, 041039 (2023), arXiv:2111.03606 [gr-qc].
 - [5] S. Vitale, D. Gerosa, W. M. Farr, and S. R. Taylor, in *Handbook of Gravitational Wave Astronomy* (Springer, 2022) pp. 1–60.
 - [6] E. Thrane and C. Talbot, *Publ. Astron. Soc. Austral.* **36**, e010 (2019), arXiv:1809.02293 [astro-ph.IM].
 - [7] T. A. Callister, (2024), arXiv:2410.19145 [astro-ph.HE].
 - [8] B. Abbott *et al.* (LIGO Scientific, Virgo), *Astrophys. J. Lett.* **882**, L24 (2019), arXiv:1811.12940 [astro-ph.HE].
 - [9] R. Abbott *et al.* (LIGO Scientific, Virgo), *Astrophys. J. Lett.* **913**, L7 (2021), arXiv:2010.14533 [astro-ph.HE].
 - [10] R. Abbott *et al.* (KAGRA, VIRGO, LIGO Scientific), *Phys. Rev. X* **13**, 011048 (2023), arXiv:2111.03634 [astro-ph.HE].
 - [11] M. Mapelli, *Front. Astron. Space Sci.* **7**, 38 (2020), arXiv:2105.12455 [astro-ph.HE].
 - [12] N. Ivanova *et al.*, *Astron. Astrophys. Rev.* **21**, 59 (2013), arXiv:1209.4302 [astro-ph.HE].
 - [13] S. S. Bavera *et al.*, *Astron. Astrophys.* **647**, A153 (2021), arXiv:2010.16333 [astro-ph.HE].
 - [14] D. Gerosa and M. Fishbach, *Nature Astron.* **5**, 8 (2021), arXiv:2105.03439 [astro-ph.HE].
 - [15] M. Mapelli, N. Giacobbo, F. Santoliquido, and M. C. Artale, *Mon. Not. Roy. Astron. Soc.* **487**, 2 (2019), arXiv:1902.01419 [astro-ph.HE].
 - [16] I. Mandel and F. S. Broekgaarden, *Living Rev. Rel.* **25**, 1 (2022), arXiv:2107.14239 [astro-ph.HE].
 - [17] E. P. J. van den Heuvel, S. F. Portegies Zwart, and S. E. de Mink, *Mon. Not. Roy. Astron. Soc.* **471**, 4256 (2017), arXiv:1701.02355 [astro-ph.SR].
 - [18] C. J. Neijssel, A. Vigna-Gómez, S. Stevenson, J. W. Barrett, S. M. Gaebel, F. Broekgaarden, S. E. de Mink, D. Szécsi, S. Vinciguerra, and I. Mandel, *Mon. Not. Roy. Astron. Soc.* **490**, 3740 (2019), arXiv:1906.08136 [astro-ph.SR].
 - [19] M. Gallegos-Garcia, C. P. L. Berry, P. Marchant, and V. Kalogera, *Astrophys. J.* **922**, 110 (2021), arXiv:2107.05702 [astro-ph.HE].
 - [20] M. M. Briel, H. F. Stevance, and J. J. Eldridge, *Mon. Not. Roy. Astron. Soc.* **520**, 5724 (2023),

- arXiv:2206.13842 [astro-ph.HE].
- [21] P. Eggleton, S. Mitton, and J. Whelan, eds., *Structure and Evolution of Close Binary Systems*, IAU Symposium, Vol. 73 (1976).
 - [22] B. Paczynski, Symposium - International Astronomical Union **73**, 75–80 (1976).
 - [23] A. V. Tutukov and L. R. YungelSon, Mon. Not. Roy. Astron. Soc. **260**, 675 (1993).
 - [24] H. A. Bethe and G. E. Brown, Astrophys. J. **506**, 780 (1998), arXiv:astro-ph/9802084.
 - [25] K. Belczynski, V. Kalogera, and T. Bulik, Astrophys. J. **572**, 407 (2002), arXiv:astro-ph/0111452 [astro-ph].
 - [26] S. Stevenson, A. Vigna-Gómez, I. Mandel, J. W. Barrett, C. J. Neijssel, D. Perkins, and S. E. de Mink, Nature Commun. **8**, 14906 (2017), arXiv:1704.01352 [astro-ph.HE].
 - [27] N. Giacobbo and M. Mapelli, Mon. Not. Roy. Astron. Soc. **480**, 2011 (2018), arXiv:1806.00001 [astro-ph.HE].
 - [28] M. Dominik, K. Belczynski, C. Fryer, D. Holz, E. Berti, T. Bulik, I. Mandel, and R. O’Shaughnessy, Astrophys. J. **759**, 52 (2012), arXiv:1202.4901 [astro-ph.HE].
 - [29] P. C. Peters, Phys. Rev. **136**, B1224 (1964).
 - [30] M. Zevin, S. S. Bavera, C. P. L. Berry, V. Kalogera, T. Fragos, P. Marchant, C. L. Rodriguez, F. Antonini, D. E. Holz, and C. Pankow, Astrophys. J. **910**, 152 (2021), arXiv:2011.10057 [astro-ph.HE].
 - [31] S. E. de Mink, M. Cantiello, N. Langer, O. R. Pols, I. Brott, and S. C. Yoon, Astron. Astrophys. **497**, 243 (2009), arXiv:0902.1751 [astro-ph.SR].
 - [32] I. Mandel and S. E. de Mink, Mon. Not. Roy. Astron. Soc. **458**, 2634 (2016), arXiv:1601.00007 [astro-ph.HE].
 - [33] S. E. de Mink and I. Mandel, Mon. Not. Roy. Astron. Soc. **460**, 3545 (2016), arXiv:1603.02291 [astro-ph.HE].
 - [34] P. Marchant, N. Langer, P. Podsiadlowski, T. M. Tauris, and T. J. Moriya, Astron. Astrophys. **588**, A50 (2016), arXiv:1601.03718 [astro-ph.SR].
 - [35] L. du Buisson, P. Marchant, P. Podsiadlowski, C. Kobayashi, F. B. Abdalla, P. Taylor, I. Mandel, S. E. de Mink, T. J. Moriya, and N. Langer, Mon. Not. Roy. Astron. Soc. **499**, 5941 (2020), arXiv:2002.11630 [astro-ph.HE].
 - [36] S. Sigurdsson and L. Hernquist, Nature **364**, 423 (1993).
 - [37] S. Sigurdsson and E. S. Phinney, Astrophys. J. **415**, 631 (1993).
 - [38] S. F. Portegies Zwart and S. McMillan, Astrophys. J. Lett. **528**, L17 (2000), arXiv:astro-ph/9910061.
 - [39] M. C. Miller and D. P. Hamilton, Astrophys. J. **576**, 894 (2002), arXiv:astro-ph/0202298.
 - [40] A. P. Lightman and S. L. Shapiro, Rev. Mod. Phys. **50**, 437 (1978).
 - [41] P. Hut, S. McMillan, J. Goodman, M. Mateo, E. S. Phinney, C. Pryor, H. B. Richer, F. Verbunt, and M. Weinberg, Publ. Astron. Soc. Pac. **104**, 981 (1992).
 - [42] J. M. Fregeau and F. A. Rasio, Astrophys. J. **658**, 1047 (2007), arXiv:astro-ph/0608261.
 - [43] R. M. O’Leary, F. A. Rasio, J. M. Fregeau, N. Ivanova, and R. W. O’Shaughnessy, Astrophys. J. **637**, 937 (2006), arXiv:astro-ph/0508224.
 - [44] J. M. B. Downing, M. J. Benacquista, M. Giersz, and R. Spurzem, Mon. Not. Roy. Astron. Soc. **407**, 1946 (2010), arXiv:0910.0546 [astro-ph.SR].
 - [45] C. L. Rodriguez, M. Morscher, B. Pattabiraman, S. Chatterjee, C.-J. Haster, and F. A. Rasio, Phys. Rev. Lett. **115**, 051101 (2015), [Erratum: Phys.Rev.Lett. **116**, 029901 (2016)], arXiv:1505.00792 [astro-ph.HE].
 - [46] C. L. Rodriguez, S. Chatterjee, and F. A. Rasio, Phys. Rev. D **93**, 084029 (2016), arXiv:1602.02444 [astro-ph.HE].
 - [47] C. L. Rodriguez, M. Zevin, P. Amaro-Seoane, S. Chatterjee, K. Kremer, F. A. Rasio, and C. S. Ye, Phys. Rev. D **100**, 043027 (2019), arXiv:1906.10260 [astro-ph.HE].
 - [48] A. Askar, M. Szkudlarek, D. Gondek-Rosińska, M. Giersz, and T. Bulik, Mon. Not. Roy. Astron. Soc. **464**, L36 (2017), arXiv:1608.02520 [astro-ph.HE].
 - [49] M. Miller and V. M. Lauburg, Astrophys. J. **692**, 917 (2009), arXiv:0804.2783 [astro-ph].
 - [50] S. Banerjee, H. Baumgardt, and P. Kroupa, Mon. Not. Roy. Astron. Soc. **402**, 371 (2010), arXiv:0910.3954 [astro-ph.SR].
 - [51] J. P. Zahn, Astron. Astrophys. **57**, 383 (1977).
 - [52] F. Antonini and F. A. Rasio, Astrophys. J. **831**, 187 (2016), arXiv:1606.04889 [astro-ph.HE].
 - [53] B. McKernan *et al.*, Astrophys. J. **866**, 66 (2018), arXiv:1702.07818 [astro-ph.HE].
 - [54] B. McKernan, K. E. S. Ford, R. O’Shaughnessy, and D. Wysocki, Mon. Not. Roy. Astron. Soc. **494**, 1203 (2020), arXiv:1907.04356 [astro-ph.HE].
 - [55] N. C. Stone, B. D. Metzger, and Z. Haiman, Mon. Not. Roy. Astron. Soc. **464**, 946 (2017), arXiv:1602.04226 [astro-ph.GA].
 - [56] H. Tagawa, Z. Haiman, and B. Kocsis, Astrophys. J. **898**, 25 (2020), arXiv:1912.08218 [astro-ph.GA].
 - [57] H. Tagawa, Z. Haiman, I. Bartos, B. Kocsis, and K. Omukai, Mon. Not. Roy. Astron. Soc. **507**, 3362 (2021), arXiv:2104.09510 [astro-ph.HE].
 - [58] I. Bartos, B. Kocsis, Z. Haiman, and S. Márka, The Astrophysical Journal **835**, 165 (2017).
 - [59] Y. Yang, I. Bartos, Z. Haiman, B. Kocsis, S. Márka, and H. Tagawa, Astrophys. J. **896**, 138 (2020), arXiv:2003.08564 [astro-ph.HE].
 - [60] H. Sana, J.-B. Le Bouquin, S. Lacour, J.-P. Berger, G. Duvert, L. Gauchet, B. Norris, J. Olofsson, D. Pickel, G. Zins, *et al.*, The Astrophysical Journal Supplement Series **215**, 15 (2014).
 - [61] K. Silsbee and S. Tremaine, Astrophys. J. **836**, 39 (2017), arXiv:1608.07642 [astro-ph.HE].
 - [62] C. L. Rodriguez and F. Antonini, Astrophys. J. **863**, 7 (2018), arXiv:1805.08212 [astro-ph.HE].
 - [63] P. Gupta, H. Suzuki, H. Okawa, and K.-i. Maeda, Phys. Rev. D **101**, 104053 (2020), arXiv:1911.11318 [gr-qc].
 - [64] S. Toonen, S. P. Zwart, A. Hamers, and D. Bandopadhyay, Astronomy & Astrophysics **640**, A16 (2020).
 - [65] C. Talbot and E. Thrane, Astrophys. J. **856**, 173 (2018), arXiv:1801.02699 [astro-ph.HE].
 - [66] M. Fishbach, D. E. Holz, and W. M. Farr, Astrophys. J. Lett. **863**, L41 (2018), arXiv:1805.10270 [astro-ph.HE].
 - [67] I. M. Romero-Shaw, E. Thrane, and P. D. Lasky, Publ. Astron. Soc. Austral. **39**, e025 (2022), arXiv:2202.05479 [astro-ph.IM].
 - [68] A. Q. Cheng, M. Zevin, and S. Vitale, Astrophys. J. **955**, 127 (2023), arXiv:2307.03129 [astro-ph.HE].
 - [69] J. W. Barrett, I. Mandel, C. J. Neijssel, S. Stevenson, and A. Vigna-Gomez, IAU Symp. **325**, 46 (2016), arXiv:1704.03781 [astro-ph.HE].
 - [70] S. R. Taylor and D. Gerosa, Phys. Rev. D **98**, 083017 (2018), arXiv:1806.08365 [astro-ph.HE].
 - [71] K. W. K. Wong, K. Breivik, K. Kremer, and T. Callister, Phys. Rev. D **103**, 083021 (2021), arXiv:2011.03564

- [astro-ph.HE].
- [72] M. Mould, D. Gerosa, and S. R. Taylor, *Phys. Rev. D* **106**, 103013 (2022), arXiv:2203.03651 [astro-ph.HE].
- [73] J. Riley and I. Mandel, *Astrophys. J.* **950**, 80 (2023), arXiv:2303.00508 [astro-ph.SR].
- [74] K. Leyde, S. R. Green, A. Toubiana, and J. Gair, *Phys. Rev. D* **109**, 064056 (2024), arXiv:2311.12093 [gr-qc].
- [75] S. Mastrogiovanni, A. Lamberts, R. Srinivasan, T. Bruel, and N. Christensen, *Mon. Not. Roy. Astron. Soc.* **517**, 3432 (2022), arXiv:2207.00374 [gr-qc].
- [76] S. Colloms, C. P. L. Berry, J. Veitch, and M. Zevin, (2025), arXiv:2503.03819 [astro-ph.HE].
- [77] Y. Bouffanais, M. Mapelli, F. Santoliquido, N. Giacobbo, G. Iorio, and G. Costa, *Mon. Not. Roy. Astron. Soc.* **505**, 3873 (2021), arXiv:2010.11220 [astro-ph.HE].
- [78] C. Plunkett, M. Mould, and S. Vitale, (2025), arXiv:2504.18615 [gr-qc].
- [79] J. Heinzl, M. Mould, S. Álvarez-López, and S. Vitale, *Phys. Rev. D* **111**, 063043 (2025), arXiv:2406.16813 [astro-ph.HE].
- [80] B. Edelman, B. Farr, and Z. Doctor, *Astrophys. J.* **946**, 16 (2023), arXiv:2210.12834 [astro-ph.HE].
- [81] J. Godfrey, B. Edelman, and B. Farr, *Cosmic Cousins: Identification of a Subpopulation of Binary Black Holes Consistent with Isolated Binary Evolution* (2023), arXiv:2304.01288 [astro-ph.HE].
- [82] J. Golomb and C. Talbot, *Phys. Rev. D* **108**, 103009 (2023), arXiv:2210.12287 [astro-ph.HE].
- [83] J. Heinzl, S. Biscoveanu, and S. Vitale, *Phys. Rev. D* **109**, 103006 (2024), arXiv:2312.00993 [astro-ph.HE].
- [84] V. Tiwari, *Class. Quant. Grav.* **38**, 155007 (2021), arXiv:2006.15047 [astro-ph.HE].
- [85] S. Rinaldi and W. Del Pozzo, *Mon. Not. Roy. Astron. Soc.* **509**, 5454 (2021), arXiv:2109.05960 [astro-ph.IM].
- [86] T. A. Callister and W. M. Farr, *A Parameter-Free Tour of the Binary Black Hole Population* (2023), arXiv:2302.07289 [astro-ph.HE].
- [87] Y.-J. Li, Y.-Z. Wang, M.-Z. Han, S.-P. Tang, Q. Yuan, Y.-Z. Fan, and D.-M. Wei, *Astrophys. J.* **917**, 33 (2021), arXiv:2104.02969 [astro-ph.HE].
- [88] A. Ray, I. Magaña Hernandez, S. Mohite, J. Creighton, and S. Kapadia, *Astrophys. J.* **957**, 37 (2023), arXiv:2304.08046 [gr-qc].
- [89] A. M. Farah, T. A. Callister, J. M. Ezquiaga, M. Zevin, and D. E. Holz, *No need to know: astrophysics-free gravitational-wave cosmology* (2024), arXiv:2404.02210 [astro-ph.CO].
- [90] A. Toubiana, M. L. Katz, and J. R. Gair, *Mon. Not. Roy. Astron. Soc.* **524**, 5844 (2023), arXiv:2305.08909 [gr-qc].
- [91] J. Sadiq, T. Dent, and M. Gieles, *Astrophys. J.* **960**, 65 (2024), arXiv:2307.12092 [astro-ph.HE].
- [92] J. Sadiq, T. Dent, and A. Lorenzo-Medina, (2025), arXiv:2502.06451 [gr-qc].
- [93] J. Sadiq, T. Dent, and A. Lorenzo-Medina, (2025), arXiv:2506.02250 [astro-ph.HE].
- [94] I. Mandel, W. M. Farr, A. Colonna, S. Stevenson, P. Tiño, and J. Veitch, *Mon. Not. Roy. Astron. Soc.* **465**, 3254 (2017), 1608.08223 [astro-ph.HE].
- [95] C. M. Fabbri, D. Gerosa, A. Santini, M. Mould, A. Toubiana, and J. Gair, *Phys. Rev. D* **111**, 104053 (2025), arXiv:2501.17233 [astro-ph.HE].
- [96] S. Rinaldi, A. Toubiana, and J. R. Gair, (2025), arXiv:2506.05153 [gr-qc].
- [97] S. S. Bavera, M. Fishbach, M. Zevin, E. Zapartas, and T. Fragos, *Astron. Astrophys.* **665**, A59 (2022), arXiv:2204.02619 [astro-ph.HE].
- [98] A. Santini, D. Gerosa, R. Cotesta, and E. Berti, *Phys. Rev. D* **108**, 083033 (2023), arXiv:2308.12998 [astro-ph.HE].
- [99] V. Baibhav, Z. Doctor, and V. Kalogera, *Astrophys. J.* **946**, 50 (2023), arXiv:2212.12113 [astro-ph.HE].
- [100] L. A. C. van Son, S. E. de Mink, T. Callister, S. Justham, M. Renzo, T. Wagg, F. S. Broekgaarden, F. Kummer, R. Pakmor, and I. Mandel, *Astrophys. J.* **931**, 17 (2022), arXiv:2110.01634 [astro-ph.HE].
- [101] M. Zevin and S. S. Bavera, *Astrophys. J.* **933**, 86 (2022), arXiv:2203.02515 [astro-ph.HE].
- [102] F. S. Broekgaarden, S. Stevenson, and E. Thrane, *Astrophys. J.* **938**, 45 (2022), arXiv:2205.01693 [astro-ph.HE].
- [103] S. S. Bavera, T. Fragos, Y. Qin, E. Zapartas, C. J. Neijssel, I. Mandel, A. Batta, S. M. Gaebel, C. Kimball, and S. Stevenson, *Astron. Astrophys.* **635**, A97 (2020), arXiv:1906.12257 [astro-ph.HE].
- [104] T. A. Callister, C.-J. Haster, K. K. Y. Ng, S. Vitale, and W. M. Farr, *Astrophys. J. Lett.* **922**, L5 (2021), arXiv:2106.00521 [astro-ph.HE].
- [105] S. Biscoveanu, T. A. Callister, C.-J. Haster, K. K. Y. Ng, S. Vitale, and W. M. Farr, *Astrophys. J. Lett.* **932**, L19 (2022), arXiv:2204.01578 [astro-ph.HE].
- [106] C. Adamcewicz and E. Thrane, *Mon. Not. Roy. Astron. Soc.* **517**, 3928 (2022), arXiv:2208.03405 [astro-ph.HE].
- [107] J. Heinzl, M. Mould, and S. Vitale, *arXiv preprint* arXiv:2406.16844 (2024).
- [108] G. Franciolini and P. Pani, *Phys. Rev. D* **105**, 123024 (2022), arXiv:2201.13098 [astro-ph.HE].
- [109] A. Ray, I. Magaña Hernandez, K. Breivik, and J. Creighton, *Searching for binary black hole subpopulations in gravitational wave data using binned Gaussian processes* (2024), arXiv:2404.03166 [astro-ph.HE].
- [110] F. Antonini, I. M. Romero-Shaw, and T. Callister, *Phys. Rev. Lett.* **134**, 011401 (2025), arXiv:2406.19044 [astro-ph.HE].
- [111] A. Hussain, M. Isi, and A. Zimmerman, (2024), arXiv:2411.02252 [astro-ph.HE].
- [112] G. Pierra, S. Mastrogiovanni, and S. Perriès, *Astron. Astrophys.* **692**, A80 (2024), arXiv:2406.01679 [gr-qc].
- [113] V. Tiwari, *Astrophys. J.* **928**, 155 (2022), arXiv:2111.13991 [astro-ph.HE].
- [114] E. Capote *et al.*, *Phys. Rev. D* **111**, 062002 (2025), arXiv:2411.14607 [gr-qc].
- [115] T. Fragos *et al.*, *Astrophys. J. Suppl.* **264**, 45 (2023), arXiv:2202.05892 [astro-ph.SR].
- [116] K. Breivik *et al.*, *Astrophys. J.* **898**, 71 (2020), arXiv:1911.00903 [astro-ph.HE].
- [117] B. Paxton, L. Bildsten, A. Dotter, F. Herwig, P. Lesaffre, and F. Timmes (MESA), *Astrophys. J. Suppl.* **192**, 3 (2011), arXiv:1009.1622 [astro-ph.SR].
- [118] B. Paxton *et al.*, *Astrophys. J. Suppl.* **208**, 4 (2013), arXiv:1301.0319 [astro-ph.SR].
- [119] B. Paxton *et al.*, *Astrophys. J. Suppl.* **220**, 15 (2015), arXiv:1506.03146 [astro-ph.SR].
- [120] B. Paxton *et al.*, *Astrophys. J. Suppl.* **234**, 34 (2018), arXiv:1710.08424 [astro-ph.SR].
- [121] B. Paxton *et al.*, *Astrophys. J. Suppl.* **243**, 10 (2019), arXiv:1903.01426 [astro-ph.SR].

- [122] E. Racine, Phys. Rev. D **78**, 044021 (2008), arXiv:0803.1820 [gr-qc].
- [123] A. Kraskov, H. Stögbauer, and P. Grassberger, Phys. Rev. E **69**, 066138 (2004).
- [124] B. C. Ross, PLOS ONE **9**, 1 (2014).
- [125] P. Laarne, M. A. Zaidan, and T. Nieminen, SoftwareX **14**, 100686 (2021).
- [126] B. P. Abbott *et al.* (KAGRA, LIGO Scientific, Virgo), Living Rev. Rel. **19**, 1 (2016), arXiv:1304.0670 [gr-qc].
- [127] B. O. O'Reilly, M. Branchesi, S. Haino, *et al.*, Noise curves used for Simulations in the update of the Observing Scenarios Paper (2022).
- [128] R. Essick and M. Fishbach, DAGnabbit! Ensuring Consistency between Noise and Detection in Hierarchical Bayesian Inference (2023), arXiv:2310.02017 [gr-qc].
- [129] G. Pratten *et al.*, Phys. Rev. D **103**, 104056 (2021), arXiv:2004.06503 [gr-qc].
- [130] N. J. Cornish, Fast Fisher Matrices and Lazy Likelihoods (2010), arXiv:1007.4820 [gr-qc].
- [131] N. J. Cornish, Phys. Rev. D **104**, 104054 (2021), arXiv:2109.02728 [gr-qc].
- [132] B. Zackay, L. Dai, and T. Venumadhav, Relative Binning and Fast Likelihood Evaluation for Gravitational Wave Parameter Estimation (2018), arXiv:1806.08792 [astro-ph.IM].
- [133] K. Krishna, A. Vijaykumar, A. Ganguly, C. Talbot, S. Biscoveanu, R. N. George, N. Williams, and A. Zimmerman, arXiv preprint arXiv:2312.06009 (2023).
- [134] G. Ashton *et al.*, Astrophys. J. Suppl. **241**, 27 (2019), arXiv:1811.02042 [astro-ph.IM].
- [135] T. J. Loredo, AIP Conf. Proc. **735**, 195 (2004), arXiv:astro-ph/0409387.
- [136] I. Mandel, W. M. Farr, and J. R. Gair, Mon. Not. Roy. Astron. Soc. **486**, 1086 (2019), arXiv:1809.02063 [physics.data-an].
- [137] V. Tiwari, Class. Quant. Grav. **35**, 145009 (2018), arXiv:1712.00482 [astro-ph.HE].
- [138] W. M. Farr, Research Notes of the AAS **3**, 66 (2019).
- [139] S. Vitale, S. Biscoveanu, and C. Talbot, Astron. Astrophys. **668**, L2 (2022), arXiv:2209.06978 [astro-ph.HE].
- [140] J. Fuller and L. Ma, Astrophys. J. Lett. **881**, L1 (2019), arXiv:1907.03714 [astro-ph.SR].
- [141] S. J. Miller, Z. Ko, T. Callister, and K. Chatziioannou, Phys. Rev. D **109**, 104036 (2024), arXiv:2401.05613 [gr-qc].
- [142] R. W. Kiendrebeogo *et al.*, Astrophys. J. **958**, 158 (2023), arXiv:2306.09234 [astro-ph.HE].
- [143] G. Papamakarios, E. Nalisnick, D. J. Rezende, S. Mohamed, and B. Lakshminarayanan, J. Machine Learning Res. **22**, 2617 (2021), arXiv:1912.02762 [stat.ML].
- [144] I. Kobyzev, S. J. D. Prince, and M. A. Brubaker, IEEE Trans. Pattern Anal. Machine Intell. **43**, 3964 (2021), arXiv:1908.09257 [stat.ML].
- [145] D. Ward, FlowJAX: Distributions and normalizing flows in Jax ([2025]).
- [146] L. Dinh, J. Sohl-Dickstein, and S. Bengio, arXiv preprint arXiv:1605.08803 (2016).
- [147] J. Besag, Journal of the Royal Statistical Society: Series B (Methodological) **36**, 192 (1974), https://academic.oup.com/jrsssb/article-pdf/36/2/192/49096627/jrsssb_36_2_192.pdf.
- [148] J. Besag and C. Kooperberg, Biometrika **82**, 733 (1995), <https://academic.oup.com/biomet/article-pdf/82/4/733/699636/82-4-733.pdf>.